Supplementary Information

An ultra-low Pt metal nitride electrocatalyst for sustainable seawater hydrogen production

Huashuai Hu[a], Zhaorui Zhang[a, b], Yaowen Zhang[e], Tiju Thomas[f], Haiying Du[d], Keke Huang[e], J. Paul Attfield[g], and Minghui Yang[a, c, *]

[a] School of Environmental Science and Technology, Dalian University of Technology, Dalian 116024, China.

[b] School of Mechanical Engineering, Dalian University of Technology, State Key Laboratory of High-performance Precision Manufacturing. Dalian 116024, China.

[c] Ningbo Institute of Materials Technology & Engineering, Chinese Academy of Sciences, Ningbo 315201, China.

[d] College of Mechanical and Electronic Engineering, Dalian Minzu University, Dalian 116600, China.

[e] State Key Laboratory of Inorganic Synthesis and Preparative Chemistry, Jilin Provincial International Cooperation Key Laboratory of Advanced Inorganic Solid Functional Materials, College of Chemistry, Jilin University, Changchun, 130012, China.

[f] Department of Metallurgical and Materials Engineering, Indian Institute of Technology Madras, Adyar, Chennai-600036, Tamil Nadu, India.

[g] Centre for Science at Extreme Conditions and School of Chemistry, University of Edinburgh, King's Buildings, Mayfield Road, Edinburgh, UK.

Email: myang@dlut.edu.cn

This PDF file includes:

Supporting text (Methods)

Scheme S1

Figures S1 to S55

Tables S1 to S10

Caption for video S1

SI References

Other supporting materials for this manuscript include the following:

Video S1 (for supporting Figure 4 in the manuscript)

Methods

Materials and chemicals. Nickel (II) nitrate hexahydrate ($Ni(NO_3)_2 \cdot 6H_2O$), ammonium molybdate (VI) tetrahydrate (($NH_4)_6Mo_7O_{24} \cdot 4H_2O$), urea ($CO(NH_2)_2$), chloroplatinic (IV) acid hexahydrate ($H_2PtCl_6 \cdot 6H_2O$), sodium chloride ($NaCl$), ethanol absolute (C_2H_5OH), hydrochloric acid (HCl), potassium hydroxide (KOH) and acetone (CH_3COCH_3) were purchased from Aladdin Reagent (Shanghai, China). Pt/C (20 wt.%) was obtained from Johnson-Matthey Corp. Nafion 117 solution (5.0 wt%) and nickel foam (NF) were bought from Sigma-Aldrich and Tianjin Yingke United Co. Ltd, respectively. The ultrapure water (HHitech) with the resistance of 18.2 MΩ cm^{-1} at 25 °C was used to prepare the solution in all experiments. The seawater is taken from the Yellow Sea off the coast of Dalian, China (38°50′343″N, 121°37′168″E).

Synthesis of NiMoO$_4$/NF precursor. Prior to the synthesis, the NF (1.5 × 2.0 cm) was thoroughly ultrasonically cleaned according to the method in the previous literature to remove impurities and surface oxides[1]. Typically, 1.5 mmol $Ni(NO_3)_2 \cdot 6H_2O$, 0.25 mmol $(NH_4)_6Mo_7O_{24} \cdot 4H_2O$ and 3.0 mmol $CO(NH_2)_2$ were dissolved in 20.0 mL distilled (DI) water with ultrasonically for 30 minutes to obtain a clear solution. Then, two pieces of NF and the above solution were transferred to a 50 mL Teflon reactor and kept at 90 °C for 8 h. At the end of the reaction the grass green product was obtained and washed several times with DI water followed by drying in a vacuum oven (the Ni:Mo molar ratio is 6:7, named as NiMoO$_4$/NF). The precursors with different Ni:Mo molar ratios (2:7, 4:7, 8:7 and 10:7) were prepared by varying the amount of metal salt precursor added.

Synthesis of Pt-NiMoO$_4$/NF sample. The NiMoO$_4$/NF precursor was immersed directly into aqueous solutions containing different Pt concentrations (0.2, 1.0, 2.0 and 4.0 mg mL^{-1}) to prepare Pt-NiMoO$_4$/NF. When the Pt solution concentration was 2.0 mg mL^{-1}, the Pt-NiMoO$_4$/NF had the best HER activity.

Synthesis of Pt-Ni@NiMoN/NF and Ni@NiMoN/NF sample. The ammonia annealing reduction procedure was used to convert Pt-NiMoO$_4$/NF to Pt-Ni@NiMoN/NF. Specifically, the Pt-Ni@NiMoN/NF was placed in a tube furnace under NH$_3$ flow (120 mL min^{-1}) at 400 °C for 2 h with a heating rate of 5 °C min^{-1}. After allowing natural cooling to ambient temperature, Argon (Ar) was passed for 2 h to expel the residual NH$_3$. The black product

obtained was noted as Pt-Ni@NiMoN/NF. For a comprehensive comparison, Ni@NiMoN/NF was prepared by direct pyrolysis of $NiMoO_4$/NF with a similar procedure of Pt-Ni@NiMoN/NF. The effect of temperature on catalyst performance was investigated by varying the pyrolysis temperature (from 300 to 600 °C). The loading amount of catalysts on NF was about 1.2 mg cm^{-2}.

Synthesis of Pt-C/NF catalysts. The Pt-C/NF catalysts were prepared according to methods previously reported in the literature[2]. Specifically, 5.0 mg Pt/C powder was ultrasonically dissolved in a mixture of DI water (750 µL), isopropyl alcohol (250 µL), and Nafion (16 µL) to form a homogeneous suspension liquid. A portion of the ink (60 µL) was evenly applied to a piece of clean NF (0.5 × 0.5 cm^2) surface and placed under an Infrared light to evaporate the liquid. The loading amount of Pt-C on NF was controlled at *ca*. 1.2 mg cm^{-2}.

Physico-chemical characterization. The nanostructure and morphology of the synthesized catalysts were obtained by SEM (HITAGHI SU5000) and TEM (JEM-F200) with an energy dispersive X-ray spectrometer was used to examine the element mapping of the catalysts. The crystal structure of the samples was analyzed by using XRD (Rigaku SmartLab 9kw) with radiation source of Cu Kα. The metals contents of the electrocatalysts were measured by inductively coupled plasma optical emission spectrometry (ICP-OES, PerkinElmer Avio 220). XPS (Thermo ESCALAB 250XI, USA) with radiation source of Al Kα (h = 1486.6 eV) was used to determine the valence state and the chemical composition of the samples. XAS of Ni K-edge and Pt L_3-edge spectra were collected at beamline BL14W1 in Shanghai Synchrotron Radiation Facility (SSRF).

Electrocatalytic Measurements. All HER performance tests of the catalysts are performed using a typical three-electrode system in 1 M KOH, 1 M KOH + X M NaCl (X = 0.5, 1.0 and 2.0) and 1 M KOH + seawater electrolytes. Figure S43 displays the prepared electrolyte, which resulted in a significant amount of insoluble white Ca^{2+} and Mg^{2+} precipitates appearing in 1 M KOH + seawater. After the precipitation process was complete, the supernatant was extracted for subsequent electrochemical tests. The obtained catalysts grown on NF, graphite rod and Hg/HgO electrode were used as the working electrode (0.5 × 0.5 cm), auxiliary electrode and reference electrode, respectively.

The distance between the working electrode and the counter electrode was maintained at approximately 3 cm (Figure S21). During the testing process, hydrogen gas was continuously flowed above the electrolyte. Reversible hydrogen electrode (RHE) calibration in 1.0 M KOH is performed in the high purity H_2 saturated electrolyte with a Pt foil as the working electrode and a Pt wire as the counter electrode. CV was run at a scan rate of 1.0 mV s^{-1}, and the average of two potentials at which the currents cross zero was taken as the thermodynamic potential for the H_2 electrode reactions. Thus, as shown in Figure S22, the potential measured against a Hg/HgO electrode was converted to the potential versus the RHE according to E (*vs*. RHE) = E (*vs*. Hg/HgO) + 0.923 V. The LSV curves of the HER were performed at the scan rate of 2 mV s^{-1}, and were compensated by *iR* drop unless otherwise stated. To obtain more accurate activity data, we followed the recommendations and experimental results from previous literature[3-6] and performed iR correction using a value of 100%. The Tafel slopes for evaluating the catalyst's kinetic process was derived from the LSV curves by using the Tafel formula:

$$\eta = a + b \times log\, j$$

where η is the overpotential, b is the Tafel slope and j is the current density. The EIS were obtained from 10 mHz – 100 KHz with a 5 mV alternating current amplitude. In order to obtain the ECSA of the as-prepared catalysts, the double-layer capacitance (C_{dl}) value proportional to it was measured by cyclic voltammetry (CV).

$$ESCA = C_{dl}/C_s$$

where C_s (40 μF cm^{-2}) is a specific capacitance for a flat surface[7, 8]. The specific activity (SA) is obtained by normalizing the electrode current to the ECSA. Furthermore, in this work, we assumed that all metal sites (Ni, Mo and Pt) exhibit HER catalytic activity, and based on the catalyst loading (1.2 mg cm^{-2}) and ICP results (Table S1), we performed mass normalization of the electrode current to calculate the mass activity (MA) of the Pt-based electrocatalysts.[9, 10] The potential range of CV is 0.067 – 0.167 V *vs.* RHE, and the scan rates are 8, 12, 16, 20 and 24 mV s^{-1}. The durability of the Pt-Ni@NiMoN/NF was evaluated by the chronopotentiometry (CP) under different constant current densities (50, 200, 500 and 1000 mA cm^{-2}). All the CP measurements in this work were performed with *iR* correction.

Computational method. All DFT calculations were performed using the Vienna Ab Initio Simulation Package (VASP 5.2)[11, 12]. In this work, interatomic interactions are described using the generalized gradient approximation (GGA) exchange correlation energy, and the Perdew-Burke-Ernzerhof pseudopotential is used for the model configuration[13]. The cut-off energy was set to 400 eV. For structure optimization and density of states (DOS) k-points located in the Brillouin-zone were chosen for (3 × 2 × 1) and (6 × 4 × 2) calculations, respectively[14]. A vacuum layer of 15 Å was added to remove interactions between adjacent flat plates with a convergence criterion of less than 0.05 eV Å^{-1} for the force present on each ion. A self-consistent energy convergence criterion of 10^{-5} eV was used. To resolve the van der Waals (vdW) interactions between the surface and gas molecules, the zero-damping DFT-D2 method was used[15]. The adsorption energy (E_{ads}) is calculated as defined below:

$$E_{ads} = E_{total} - E_{salb} - E_{gas}$$

where E_{total}, E_{salb} and E_{gas} are the total energy of the adsorbed state structure, the energy of the independent state structure and the energy of the gas molecules, respectively. In order to study the charge transfer between the gas molecules and the material and to calculate the charge information of these most stable adsorbed structures, the charge density difference is calculated by the following equation:

$$\Delta\rho = \rho_{total} - (\rho_{salb} + \rho_{gas})$$

where ρ_{total}, ρ_{salb} and ρ_{gas} denote the total charge density, the original structural charge density and the gas molecular charge density of the system, respectively. The free energy of the HER process is calculated by the following equation:

$$\Delta G = \Delta E + \Delta E_{ZPE} - T\Delta S$$

where ΔE is the adsorption energy of a given group, ΔE_{ZPE} and ΔS are the zero-point energy difference and entropy difference between the adsorbed and corresponding independent states, respectively.
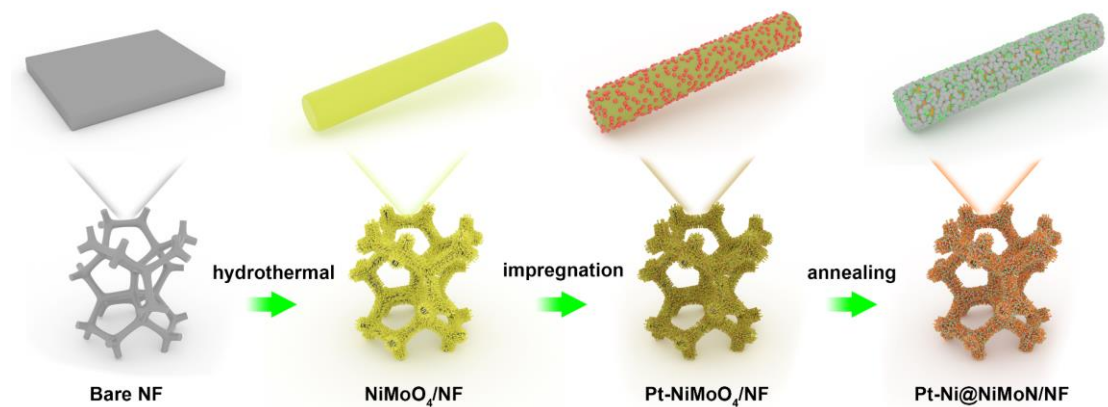
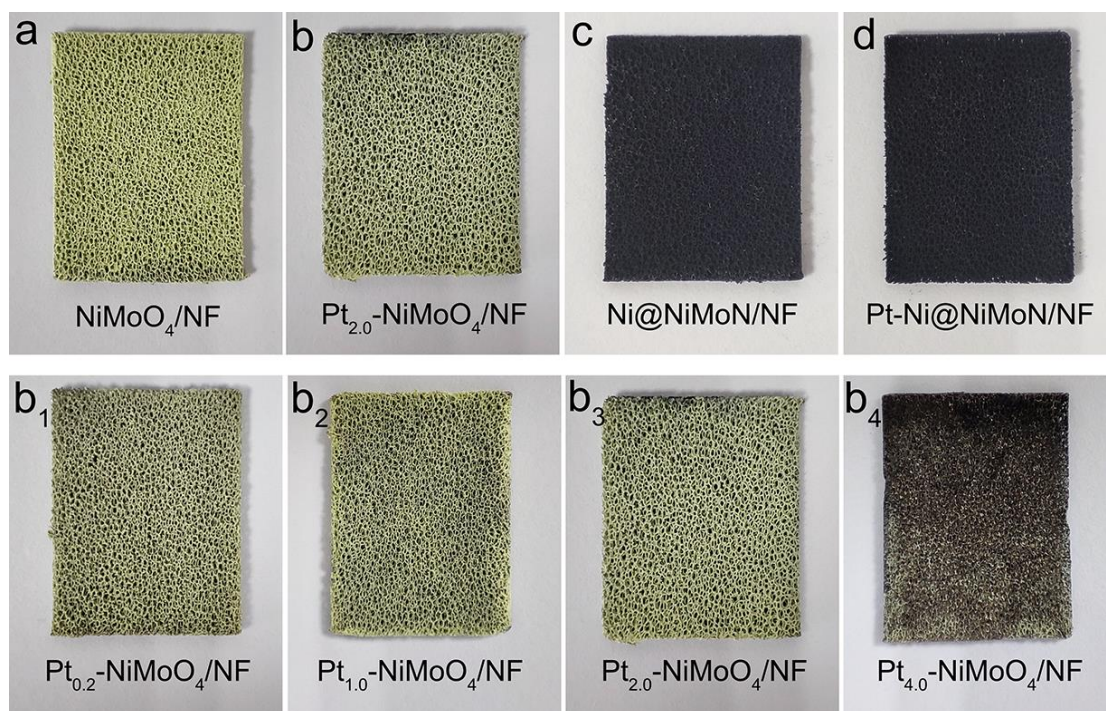**Scheme S1.** Schematic diagram of the synthesis process of Pt-Ni@NiMoN/NF.

Figure S1. a-d) Photographs of $NiMoO_4/NF$, Pt_x-$NiMoO_4/NF$ (x = 0.2, 1.0, 2.0 and 4.0), $Ni@NiMoN/NF$ and Pt-$Ni@NiMoN/NF$.

$NiMoO_4 \cdot H_2O$ precursors were grown *in-situ* on the surface of NF. Subsequently, the $NiMoO_4 \cdot H_2O$ precursors were immersed in a solution of H_2PtCl_6 at a concentration of 2.0 mg mL^{-1} to introduce the Pt element. Finally, Pt-$Ni@NiMoN/NF$ was obtained by annealing in a tube furnace by employing ammonia gas flow. Digital photographs of all samples are shown in Figure S1, the samples before and after annealing is clearly different in color, with the unannealed samples appearing grass-green and the annealed samples appearing black. It is interesting to note that as the concentration of the platinum solution increases, the original grass-green color is gradually replaced by black, indicating a high loading of Pt. The ICP results for the different catalysts are show in Table S1.

Table S1. The ICP results (mass fraction, wt%) of catalysts prepared with different Pt solution concentrations*

Catalysts	Ni	Mo	Pt
$Pt_{0.2}$-Ni@NiMoN/NF	44.62	40.51	$0.58*10^{-2}$
$Pt_{1.0}$-Ni@NiMoN/NF	44.38	39.92	$0.28*10^{-1}$
$Pt_{2.0}$-Ni@NiMoN/NF	43.12	39.15	0.07
$Pt_{4.0}$-Ni@NiMoN/NF	43.66	38.97	0.16

* The linearity of the ICP standard curve is higher than 0.9995.
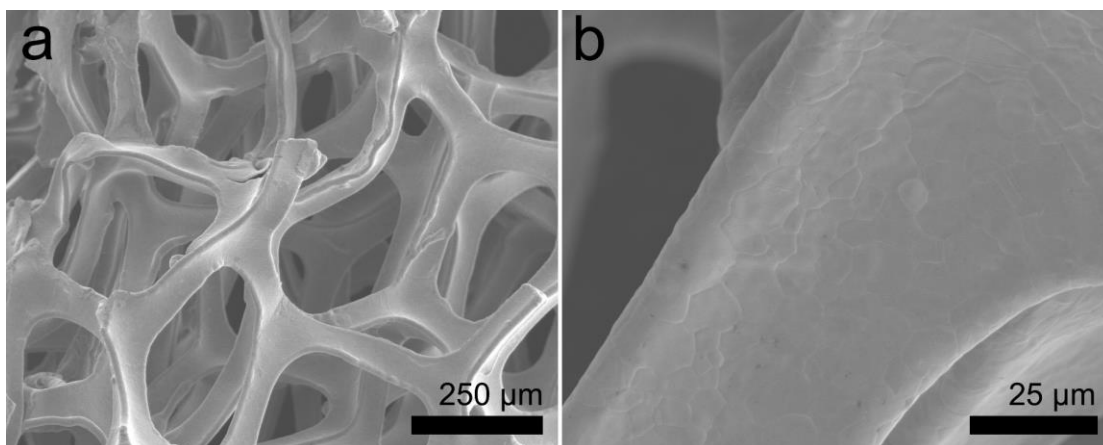
Figure S2. SEM images of bare NF.

The surface of the bare NF is found to be flat and smooth (Figure S2).
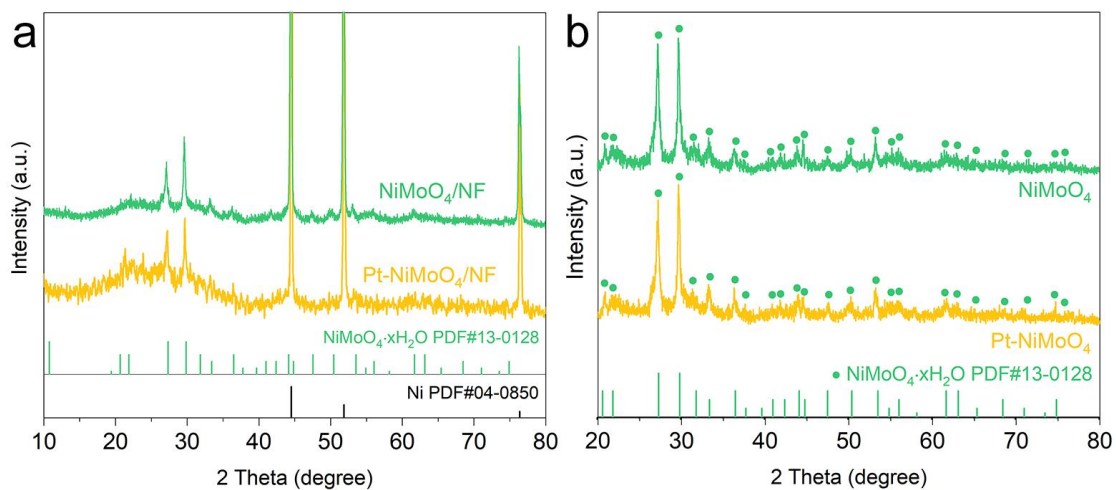
Figure S3. a) XRD pattern of NiMoO$_4$/NF and Pt-NiMoO$_4$/NF. b) XRD patterns of the powder scraped from the NiMoO$_4$/NF and Pt-NiMoO$_4$/NF.

The crystalline structure of the precursors was first investigated using powder XRD, as shown in Figure S3. To avoid the influence of the NF substrate on the diffraction peaks of the target product, the scraped off powder was also tested. All test results invariably confirm the successful preparation of NiMoO$_4 \cdot$xH$_2$O.
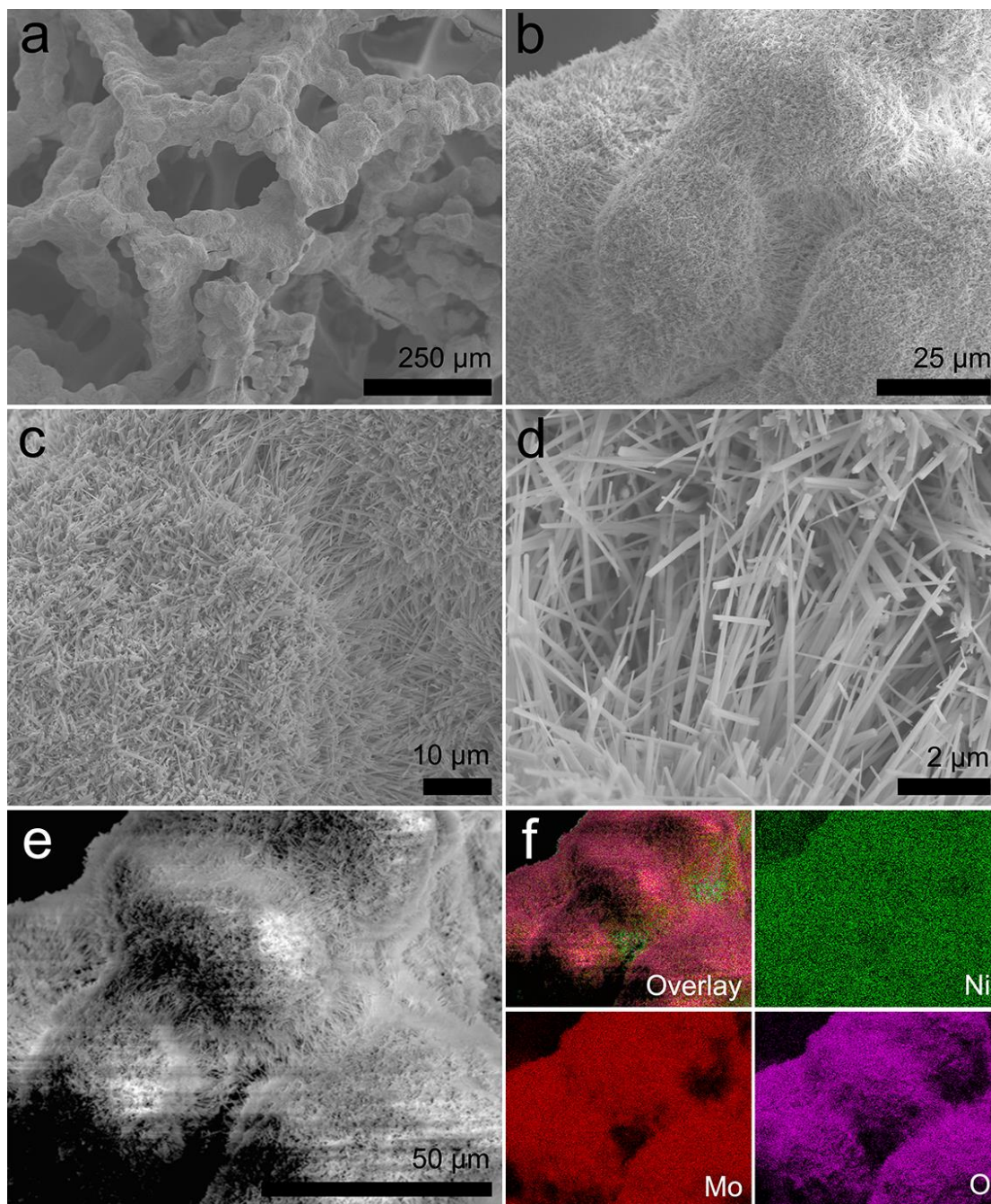
Figure S4. a-e) SEM images of NiMoO$_4$/NF. f) EDS elemental mapping of Ni, Mo and O in NiMoO$_4$/NF.

The SEM results in Figure S4 show that the NiMoO$_4$ had grown *in-situ* onto the NF surface in the form of nanorods after the hydrothermal reaction.
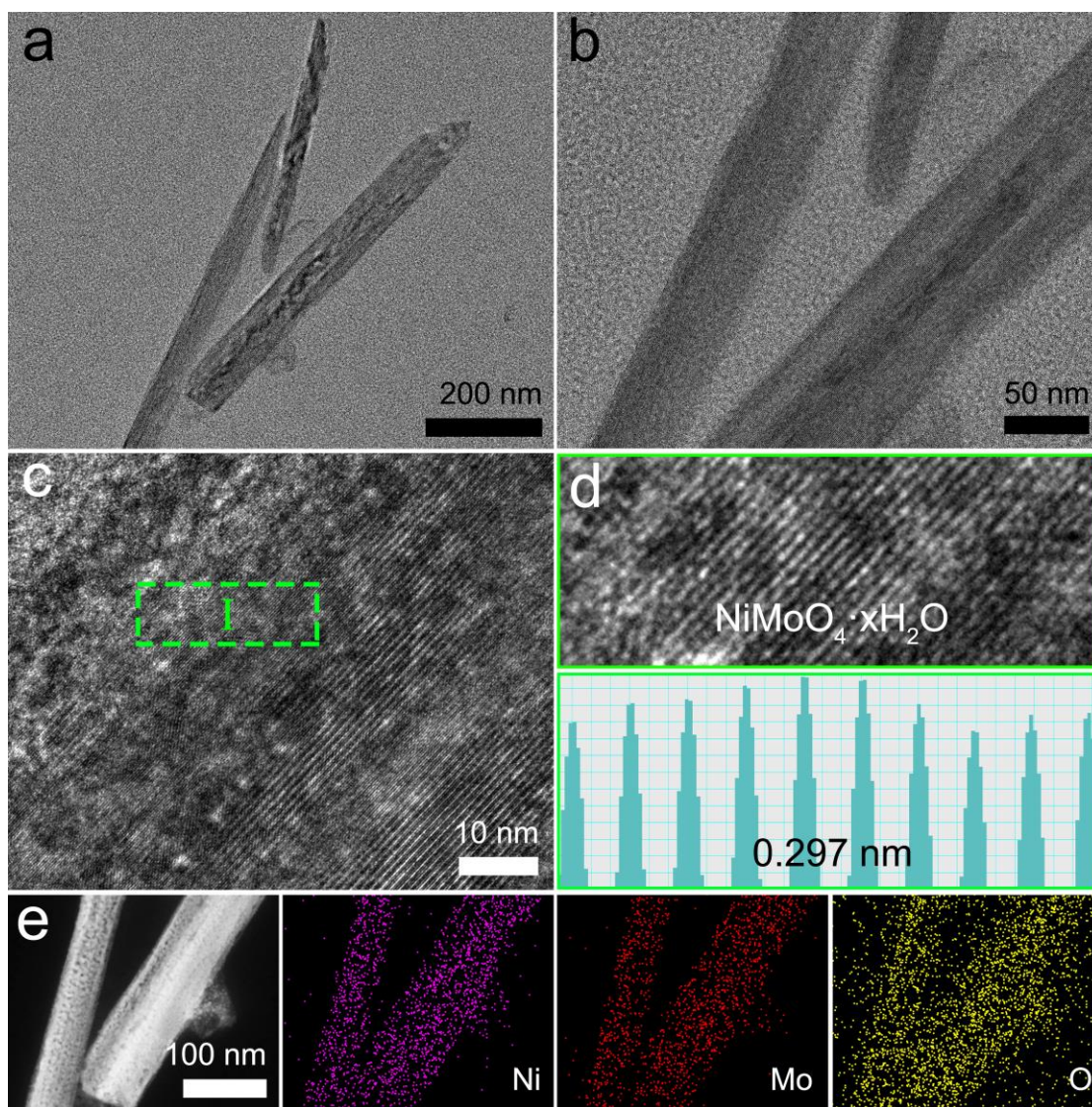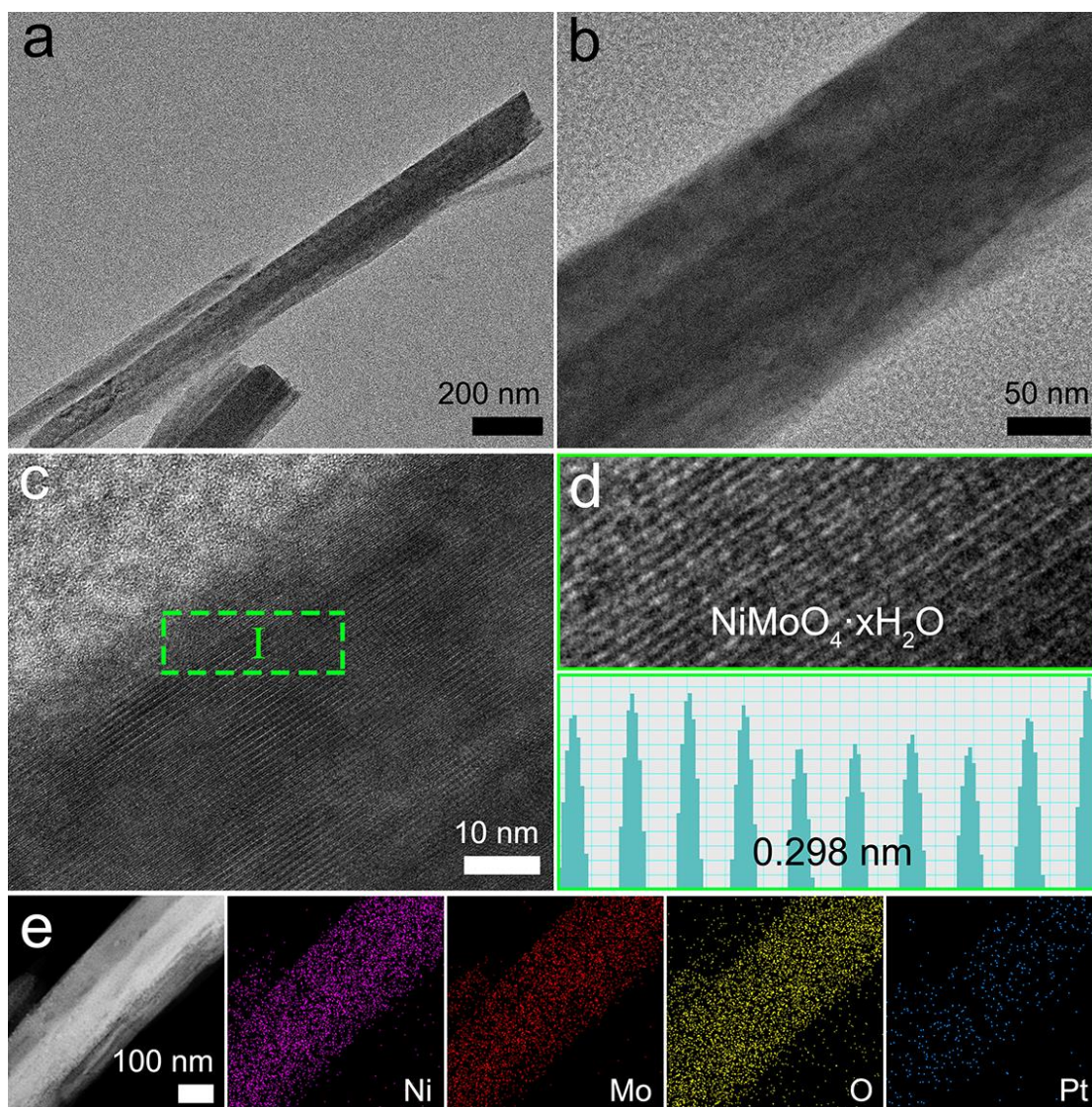
Figure S5. a-d) TEM and HRTEM images of $NiMoO_4$/NF. Interplanar spacings of the lattice fringes shown in (d). e) HAADF-STEM image and the corresponding EDS elemental mapping of Ni, Mo and O in $NiMoO_4$/NF.

TEM and high-resolution TEM (HRTEM) images (Figure S5) show that $NiMoO_4$ nanorods were highly crystalline. These samples had homogeneous elemental distribution and long range ordered lattice stripes (the crystalline plane spacing is 0.297 nm).
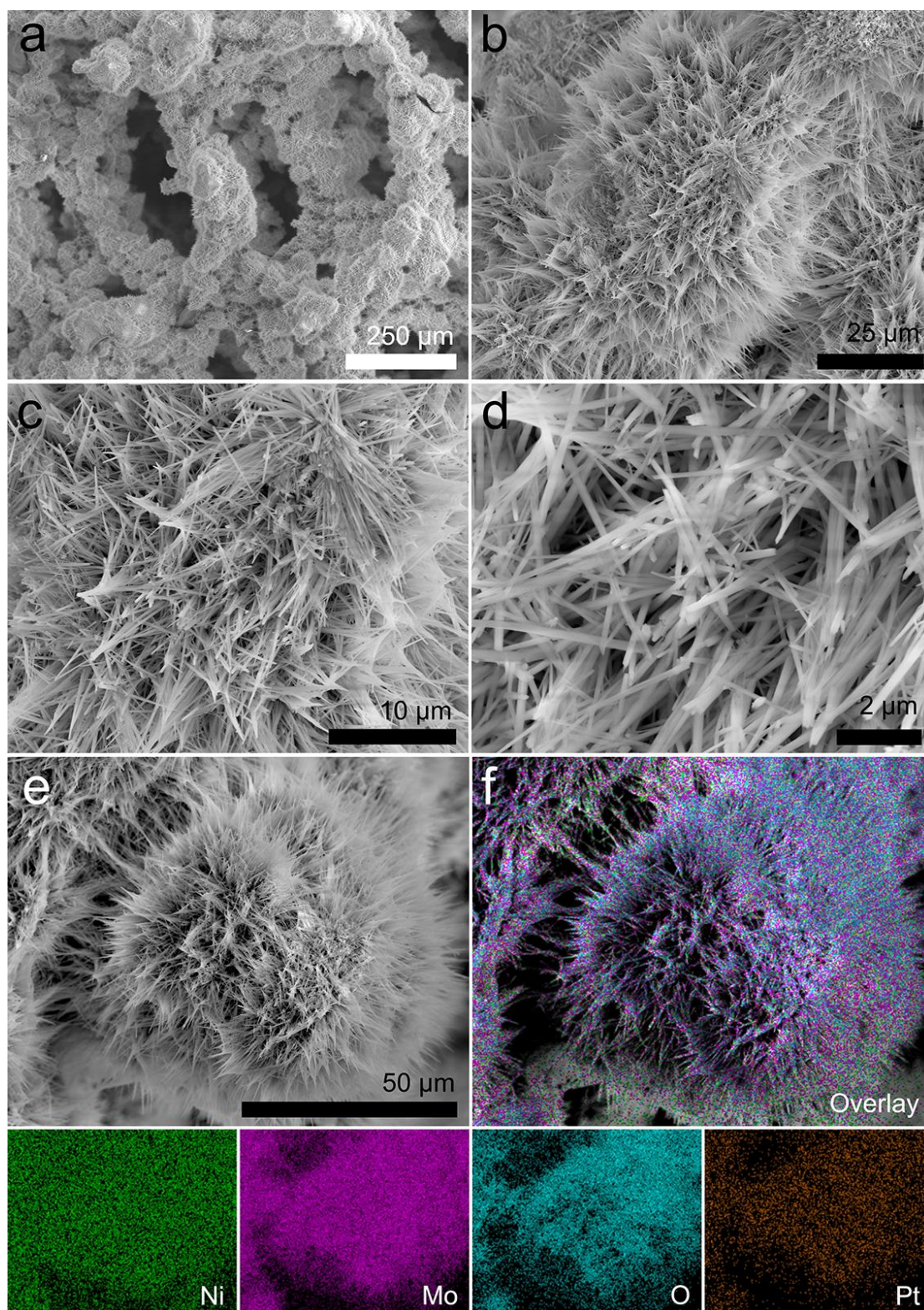
**Figure S6.** a-e) SEM images of Pt-NiMoO₄/NF. f) EDS elemental mapping of Ni, Mo, O and Pt in Pt-NiMoO₄/NF.
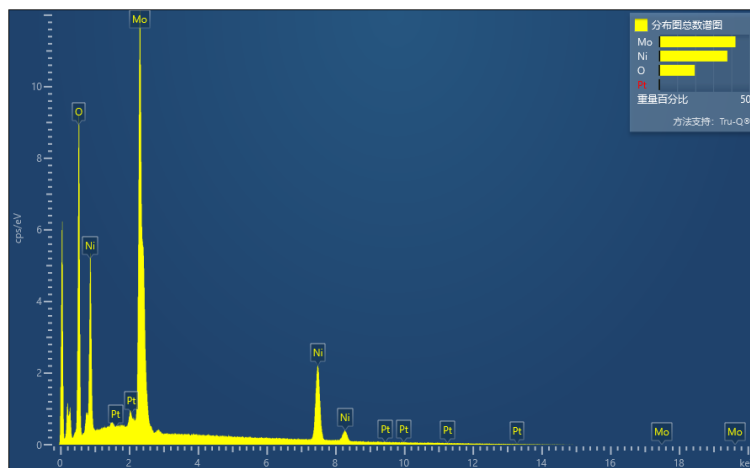
Figure S7. SEM EDS spectra of Pt-NiMoO$_4$/NF.

Table S2. The element mass fraction of Pt-NiMoO$_4$/NF obtained by SEM EDS spectra

Element	O	Ni	Mo	Pt
Family	K	K	L	M
Mass Fraction (%)	19.72	37.82	42.29	0.17

Figure S8. a-d) TEM and HRTEM images of Pt-NiMoO$_4$/NF. Interplanar spacings of the lattice fringes shown in (d). e) HAADF-STEM image and the corresponding EDS elemental mapping of Ni, Mo, O and Pt in Pt-NiMoO$_4$/NF.

The crystal structure and morphology (Figure S6-S8) of the precursor was maintained even after the introduction of the Pt element by wet chemistry. Energy-dispersive spectroscopy (EDS) shows that Pt was indeed uniformly distributed in the NiMoO$_4$ nanorod structure.
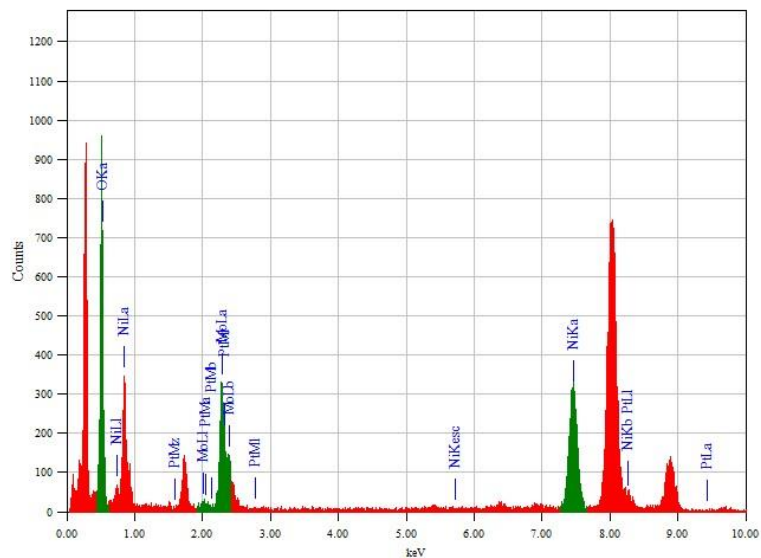
Figure S9. TEM EDS spectra of Pt-NiMoO$_4$/NF.

Table S3. The element atomic and mass fraction of Pt-NiMoO$_4$/NF obtained by TEM EDS spectra

Element	Family	keV	Atomic Fraction (%)	Mass Fraction (%)
O	K	0.525	68.99	31.78
Ni	K	7.471	16.41	27.85
Mo	L	2.293	14.55	40.21
Pt	M	2.048	0.05	0.16
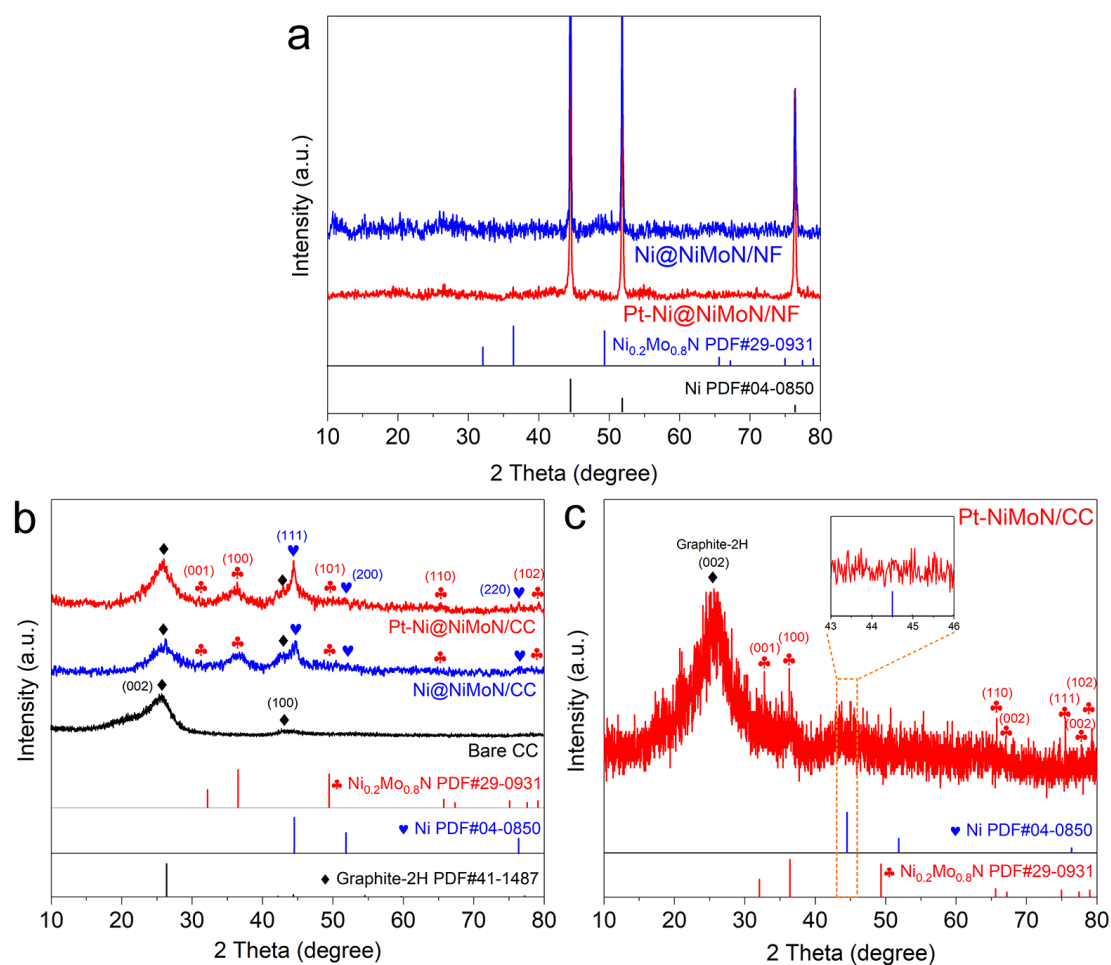
Figure S10. a) XRD pattern of Ni@NiMoN/NF and Pt-Ni@NiMoN/NF. b) XRD patterns of Bare CC, Ni@NiMoN/CC and Pt-Ni@NiMoN/CC. c) XRD pattern of Pt-Ni@NiMoN/CC after acid washing with 0.5 M H_2SO_4 for 1.0 h (named as Pt-NiMoN/CC).

As the strong characteristic peaks of the NF substrate masked the signal of the products (Figure S10a), we determined the annealed sample crystal structure by characterizing the scraped powder and replacing NF with carbon cloth (CC). After acid washing of the Ni@NiMoN/NF in dilute sulphuric acid (0.5 M) for 1 h, we observed the disappearance of the characteristic peak at 44.5° (Figure S10c). This indicates that Ni@NiMoN/NF contains metallic Ni rather than nickel nitride (Ni_3N) species[16].
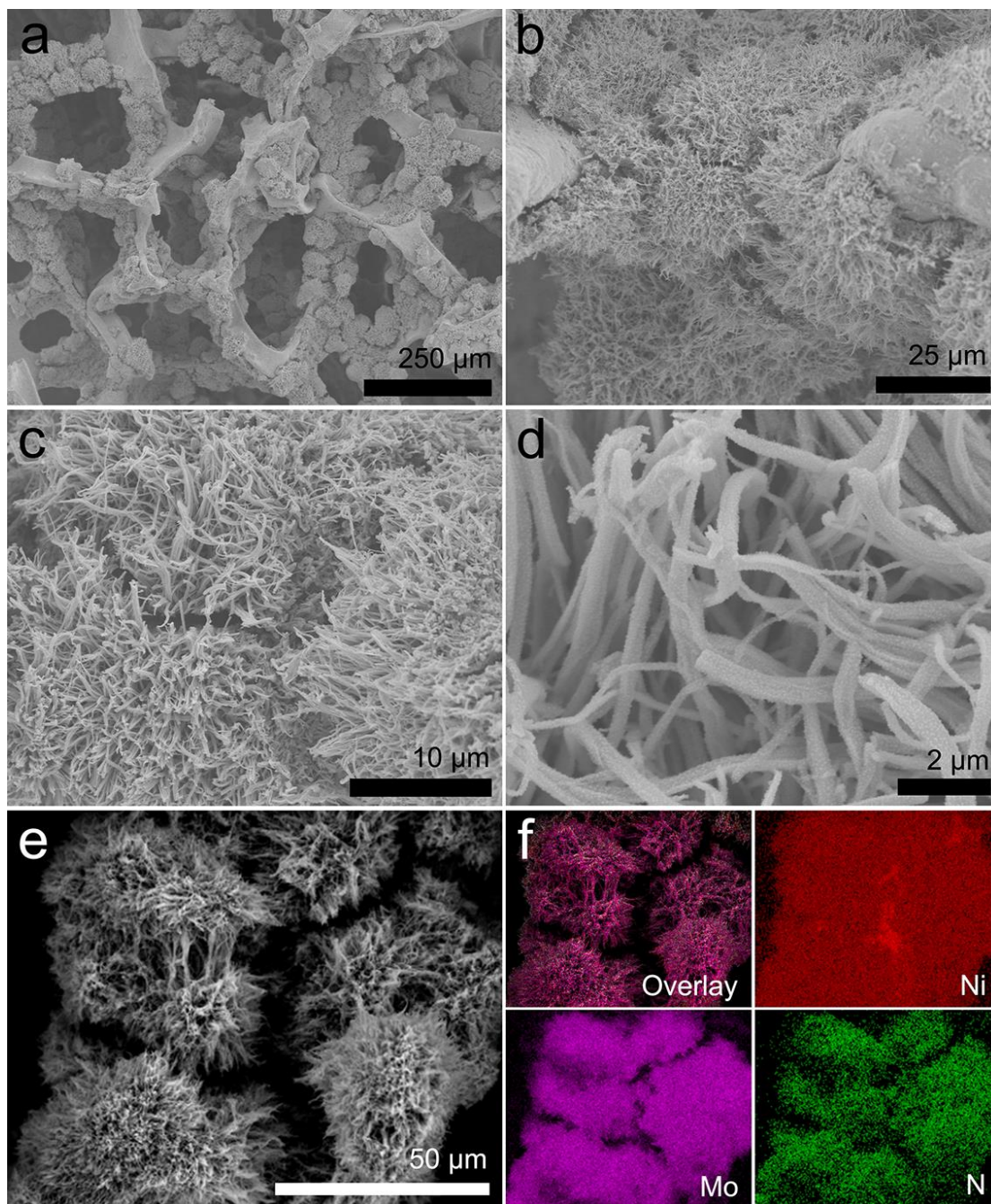
Figure S11. a-e) SEM images of Ni@NiMoN/NF. f) EDS elemental mapping of Ni, Mo and N in Ni@NiMoN/NF.

After annealing, the SEM images (Figure S11) showed that the main nanorod structure was well preserved and a large number of newly formed nanoparticles were found on the surface of the nanorods.
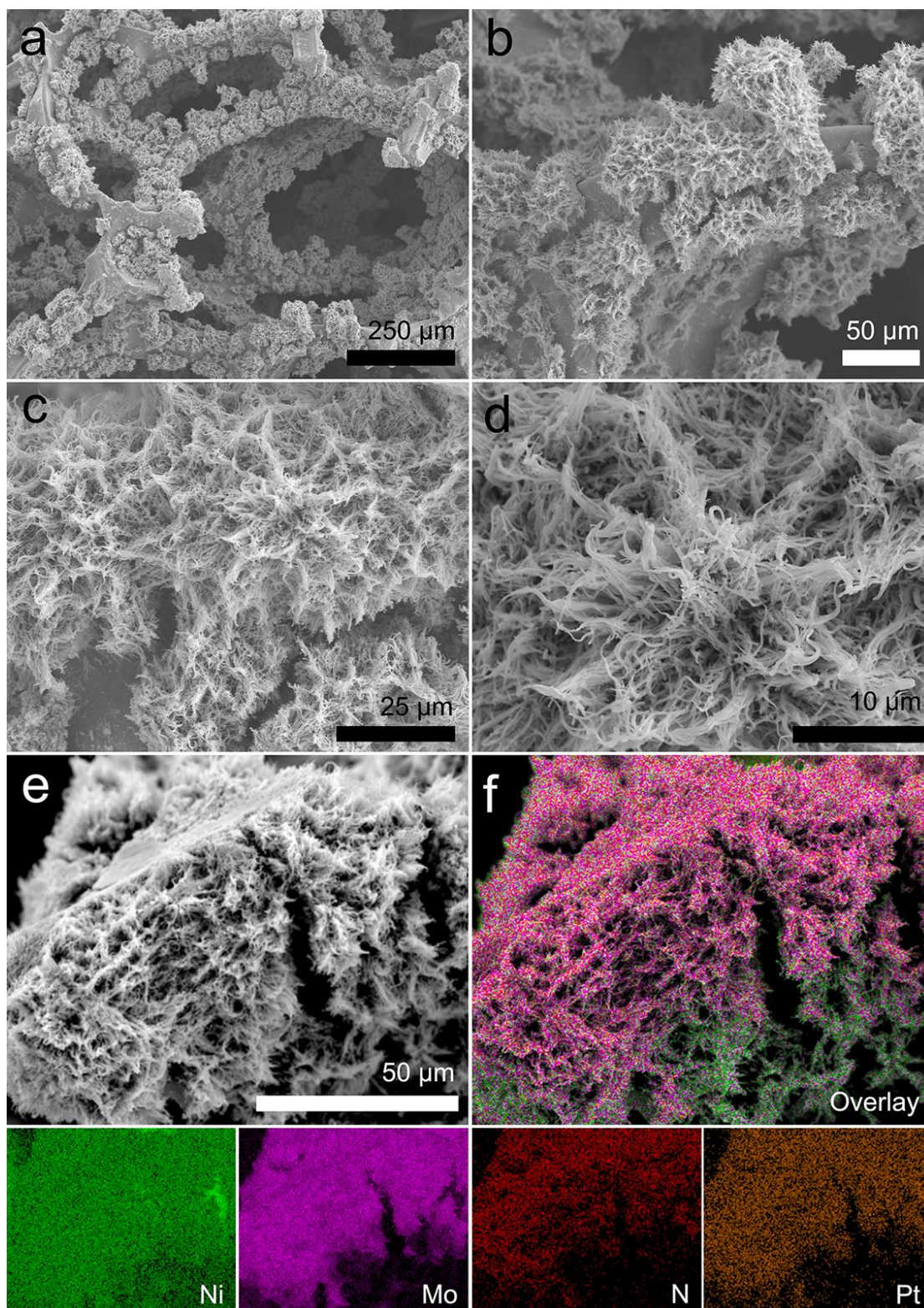
Figure S12. a-e) Low magnification SEM images of Pt-Ni@NiMoN/NF. f) EDS elemental mapping of Ni, Mo, N and Pt in Pt-Ni@NiMoN/NF.
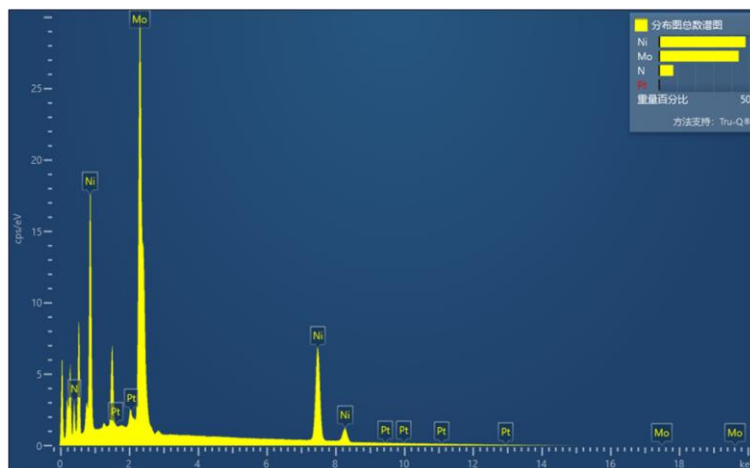
Figure S13. SEM EDS spectra of Pt-Ni@NiMoN/NF.

Table S4. The element mass fraction of Pt-Ni@NiMoN/NF obtained by SEM EDS spectra

Element	N	Ni	Mo	Pt
Family	K	K	L	M
Mass Fraction (%)	7.85	47.87	44.17	0.11
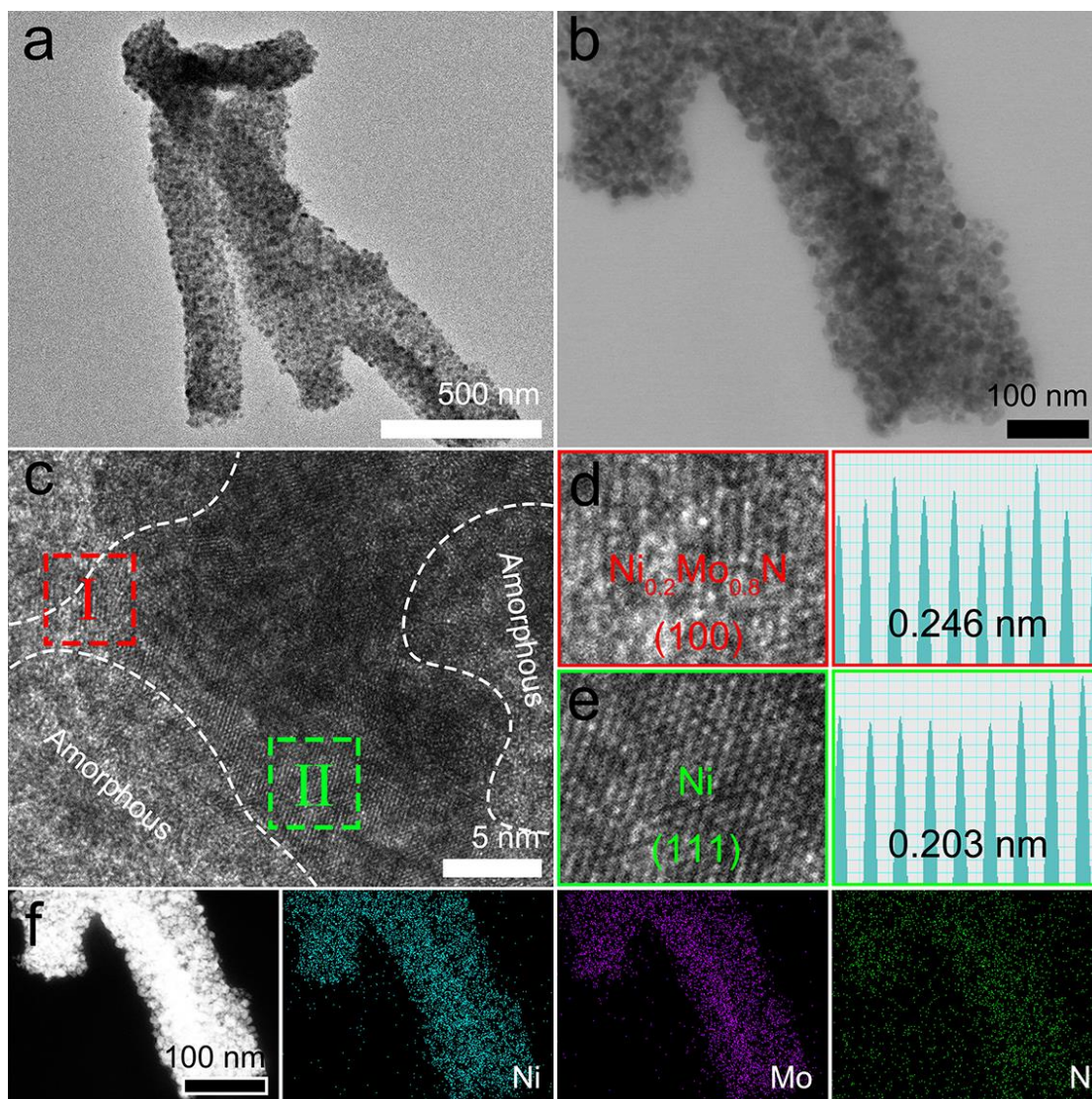
Figure S14. a-e) TEM and HRTEM images of Ni@NiMoN/NF. Interplanar spacings of the lattice fringes shown in (d-e). f) HAADF-STEM image and the corresponding EDS elemental mapping of Ni, Mo and N in Ni@NiMoN/NF.

TEM, HRTEM and EDS line scan and mapping scan were used to further determine the composition of the nanoparticles and nanorods.
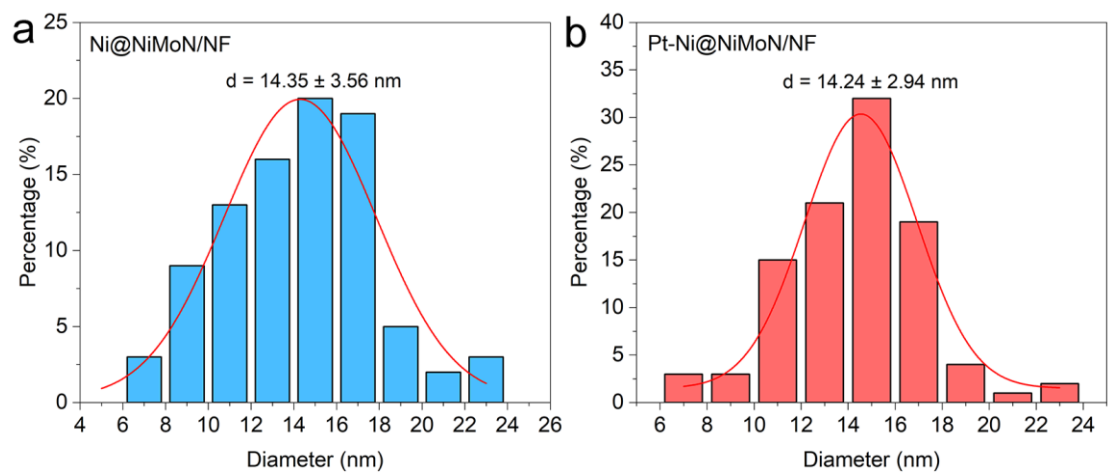
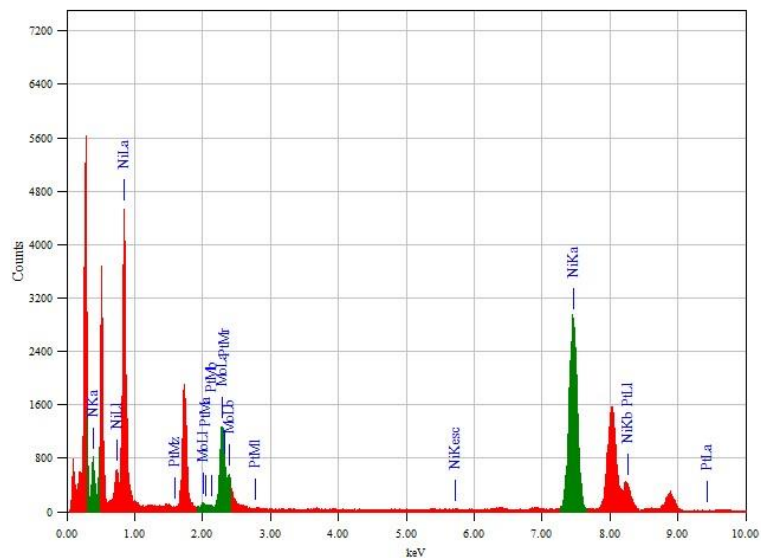**Figure S15.** Diameter distributions of the Ni nanoparticles with Gaussian fit in Ni@NiMoN/NF and Pt-Ni@NiMoN/NF.

Figure S16. TEM EDS spectra of Pt-Ni@NiMoN/NF.

Table S5. The element atomic and mass fraction of Pt-Ni@NiMoN/NF obtained by TEM EDS spectra

Element	Family	keV	Atomic Fraction (%)	Mass Fraction (%)
N	K	0.392	32.67	8.96
Ni	K	7.471	48.79	56.09
Mo	L	2.293	18.49	34.82
Pt	M	2.048	0.06	0.13
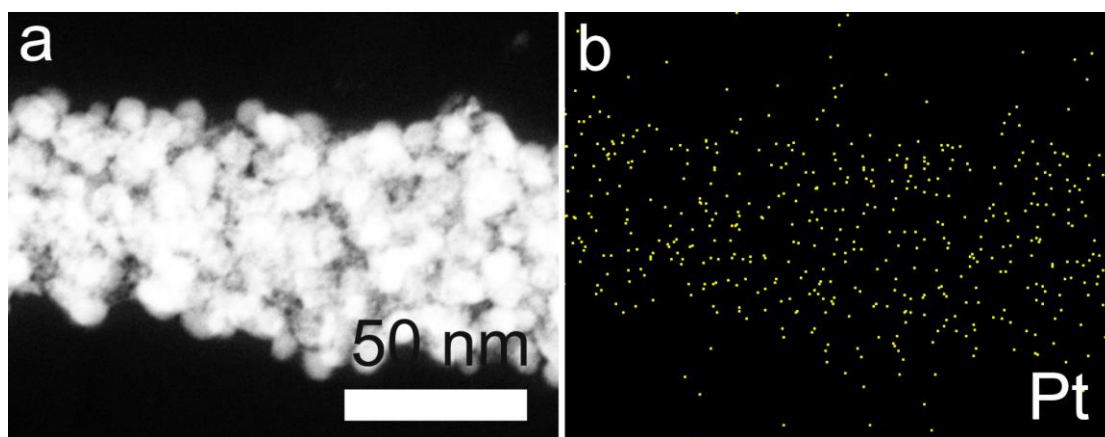
Figure S17. HAADF-STEM image of Pt-Ni@NiMoN and the corresponding element dispersion for Pt.
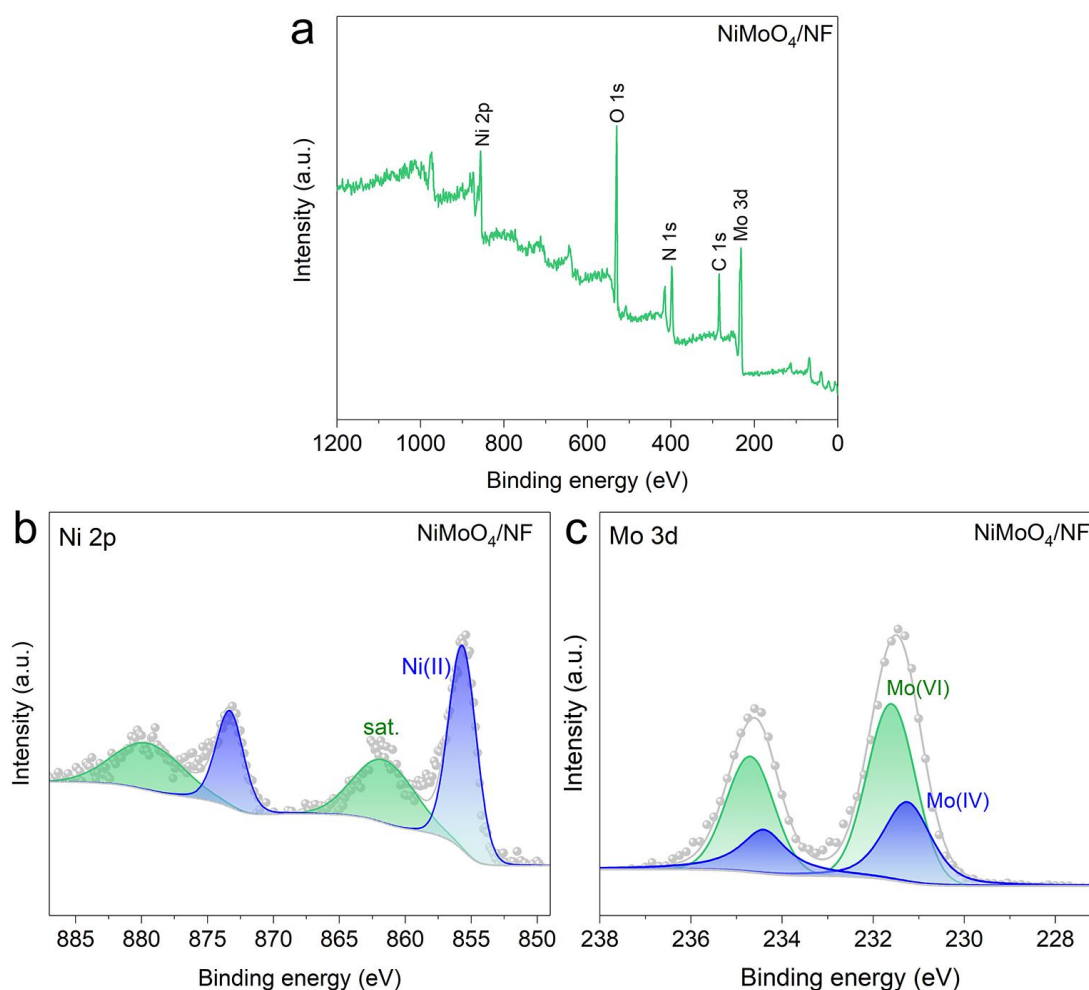
Figure S18. a) Full range XPS spectrum. b, c) High-resolution XPS spectra of Ni 2p and Mo 3d of NiMoO₄/NF.

We further investigated the surface chemical state of elemental Ni, Mo, Pt, O and N in these samples. XPS characterization was carried out. The full range XPS pattern of precursor NiMoO₄/NF confirmed the presence of Ni, Mo and O elements (Figure S18a). The high-resolution Ni 2p spectrum in Figure S18b showed two intense peaks located at 855.6 and 873.3 eV, corresponding to the Ni (II) $2p_{3/2}$ and Ni (II) $2p_{1/2}$, respectively[1, 17]. In the Mo 3d spectrum (Figure S18c), the Mo (IV) and Mo (VI) were detected.
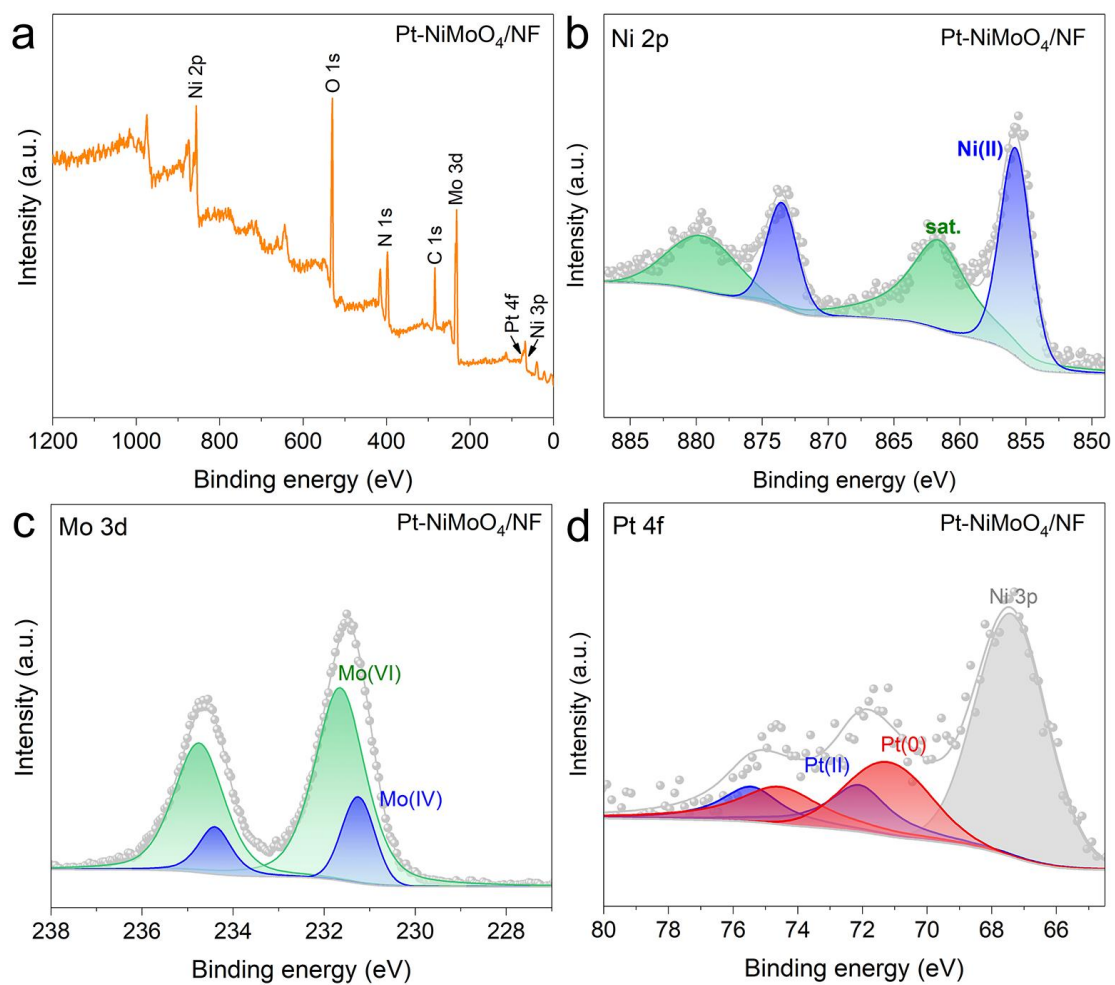
Figure S19. a) Full range XPS spectrum. b-d) High-resolution XPS spectra of Ni 2p, Mo 3d and Pt 4f of Pt-NiMoO₄/NF.
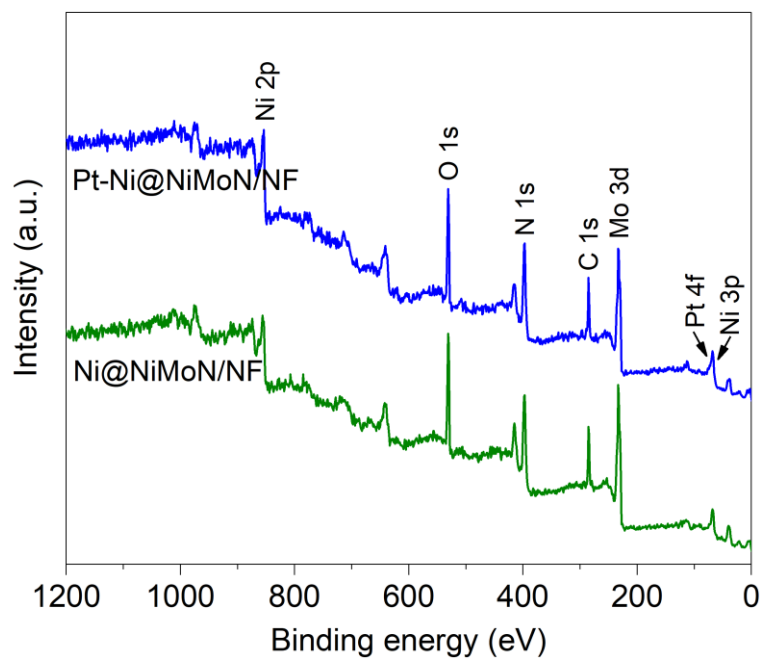
Figure S20. Full range XPS spectra of Ni@NiMoN/NF and Pt-Ni@NiMoN/NF.

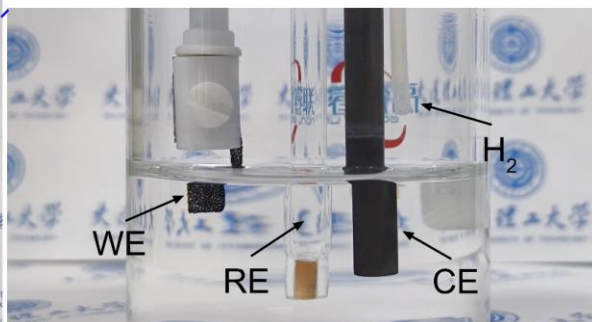WE: Work electrode
RE: Reference electrode
CE: Counter electrode

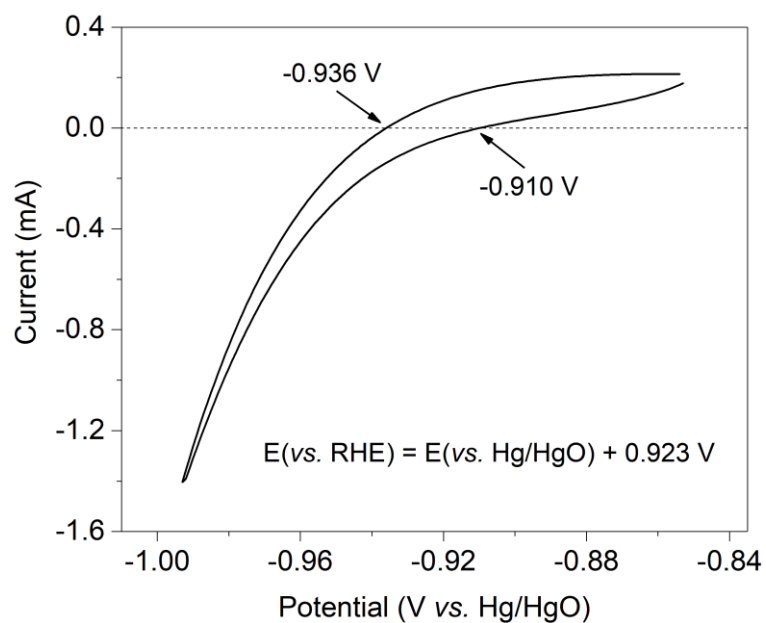**Figure S21.** Digital photograph of a single-cell three-electrode setup.

Figure S22. CV curves for RHE calibration in H_2-saturated 1.0 M KOH at 1.0 mV s^{-1}.

Prior to all electrochemical tests, the reference electrodes were calibrated to obtain reliable data (Figure S22).
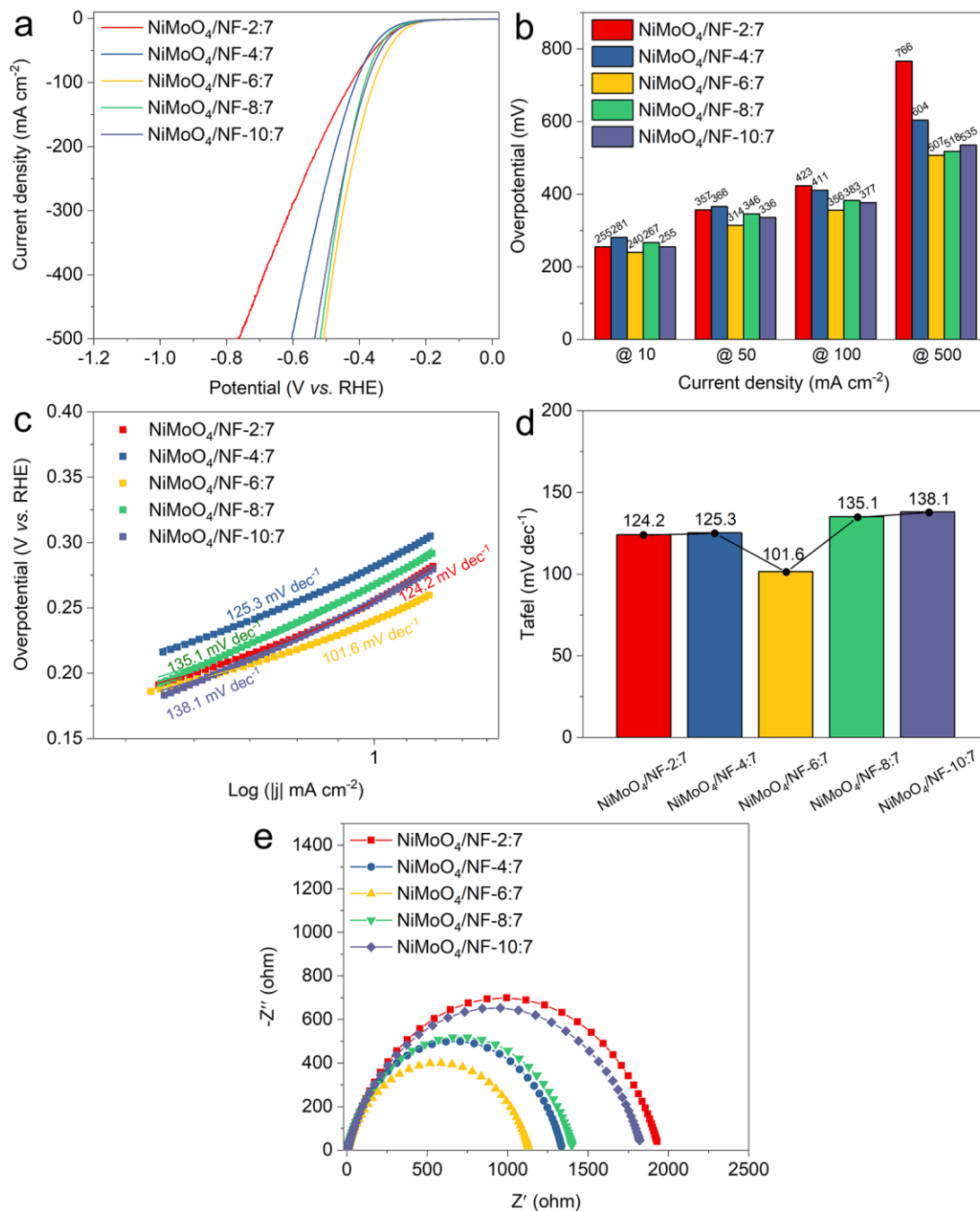
Figure S23. a) LSV curves. c) Tafel plots. e) EIS of NiMoO$_4$/NF precursors with different Ni:Mo ratios of 2:7, 4:7, 6:7, 8:7 and 10:7 for HER. Comparison of the (b) overpotentials and (d) Tafel slopes of these catalysts.
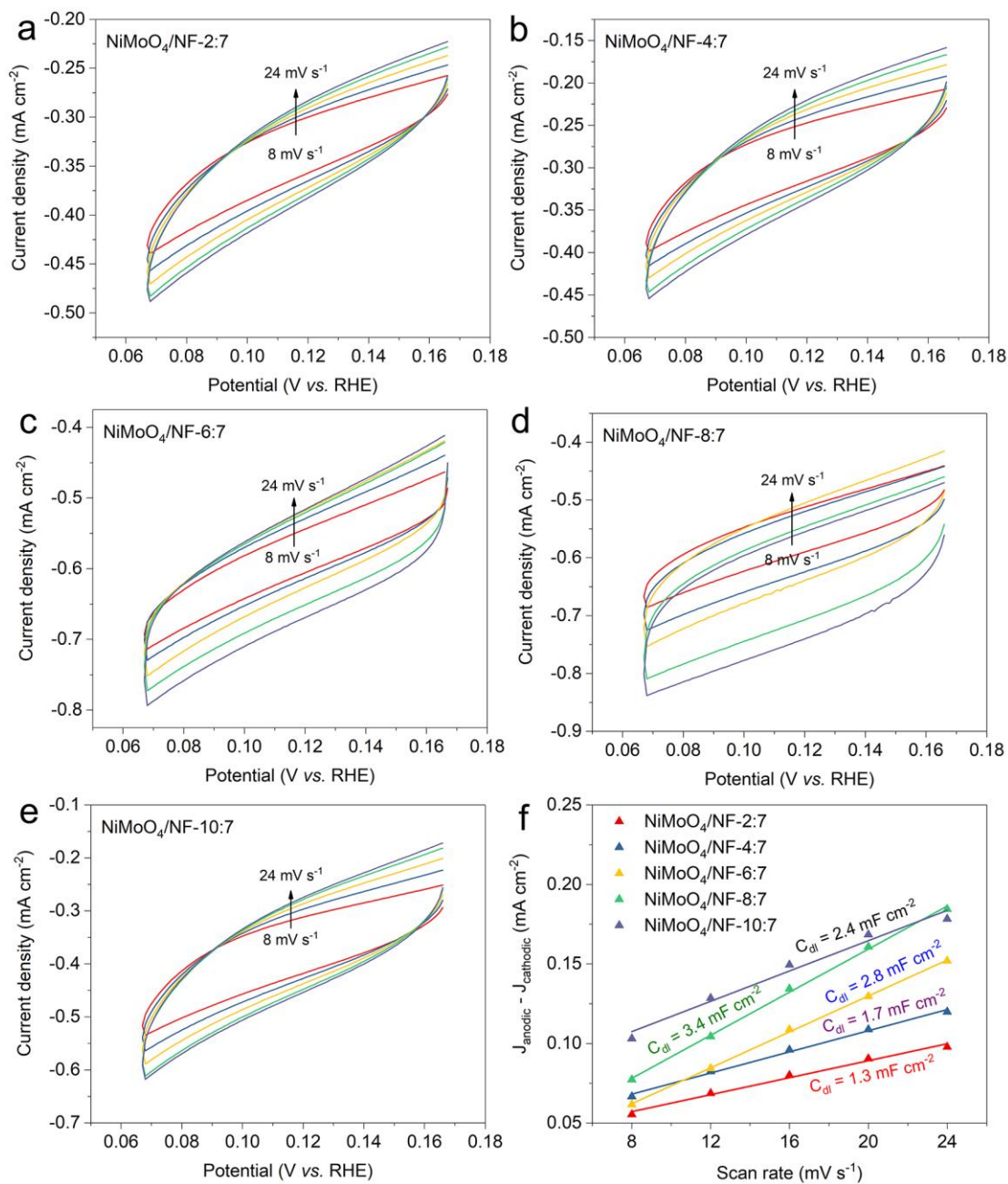
Figure S24. a-e) CV curves of NiMoO$_4$/NF precursors with different Ni:Mo ratios of 2:7, 4:7, 6:7, 8:7 and 10:7 at different scan rates in a non-faradaic potential region. f) Corresponding C_{dl} values of these catalysts.
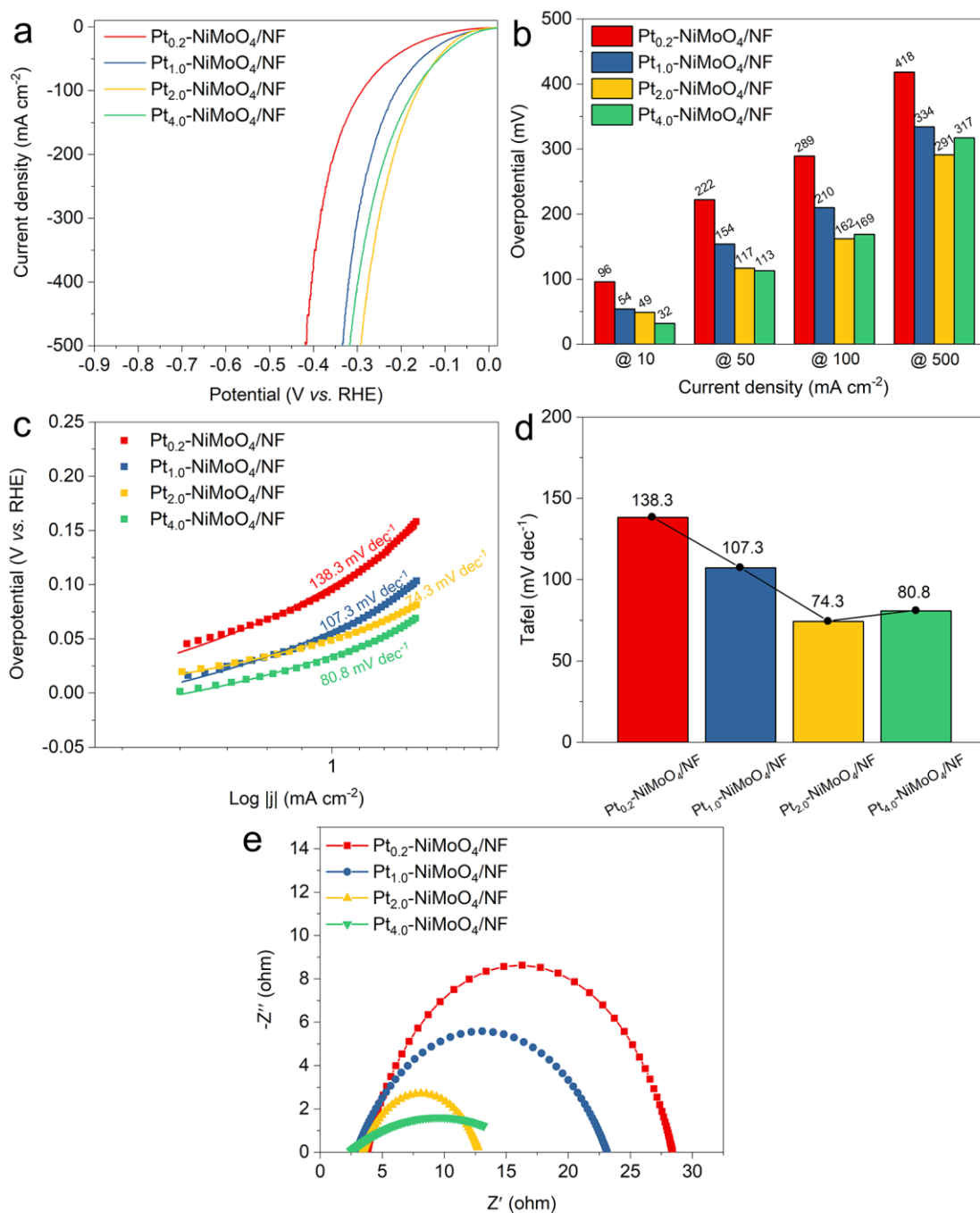
Figure S25. a) LSV curves. c) Tafel plots. e) EIS of Pt-NiMoO₄/NF precursors with different Pt solution concentrations of 0.2, 1.0, 2.0 and 4.0 mg mL⁻¹ for HER. Comparison of the (b) overpotentials and (d) Tafel slopes of these catalysts.
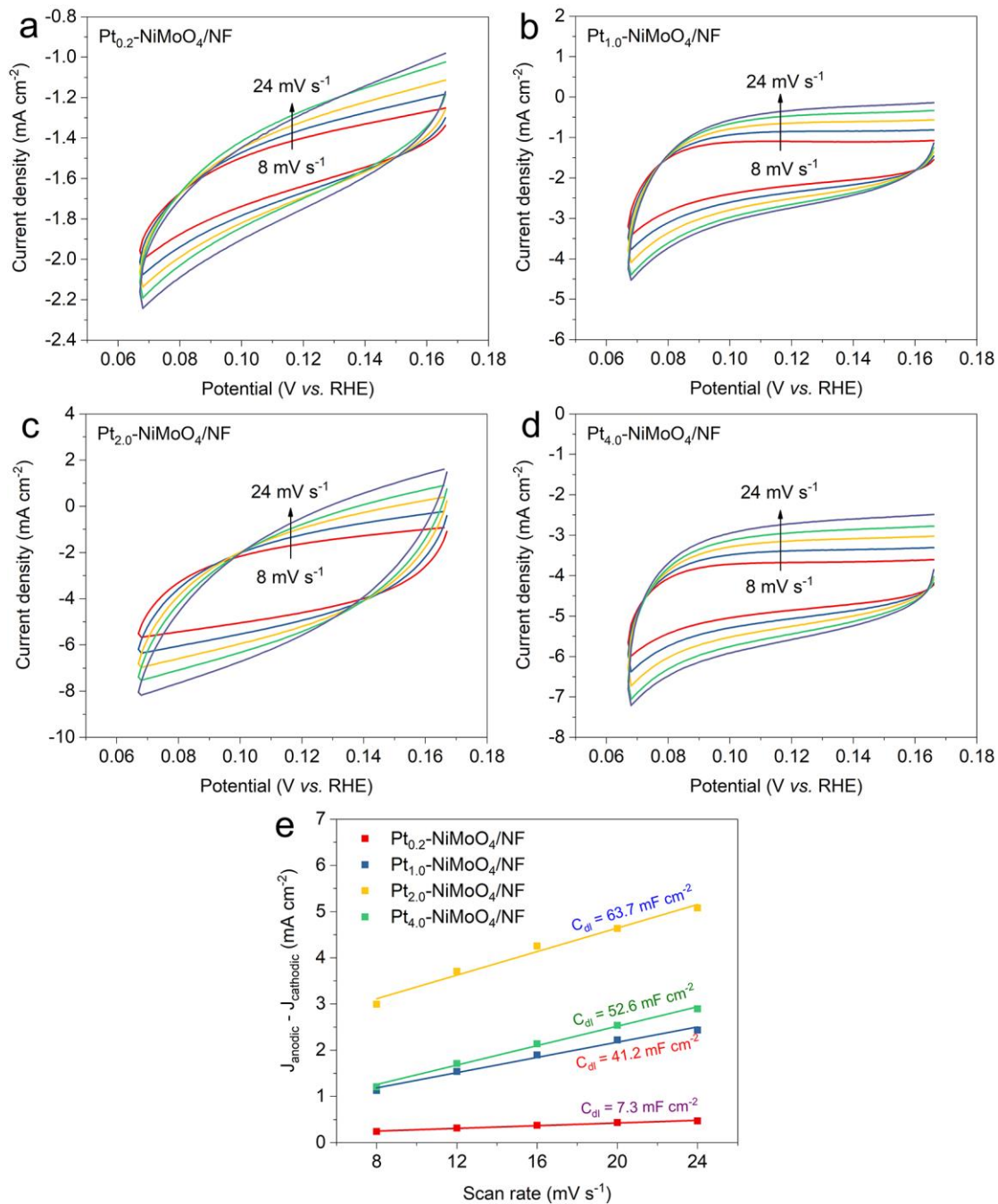
Figure S26. a-d) CV curves of Pt-NiMoO₄/NF precursors with different Pt solution concentrations of 0.2, 1.0, 2.0 and 4.0 mg ml⁻¹ at different scan rates in a non-faradaic potential region. e) Corresponding C_{dl} values of these catalysts.
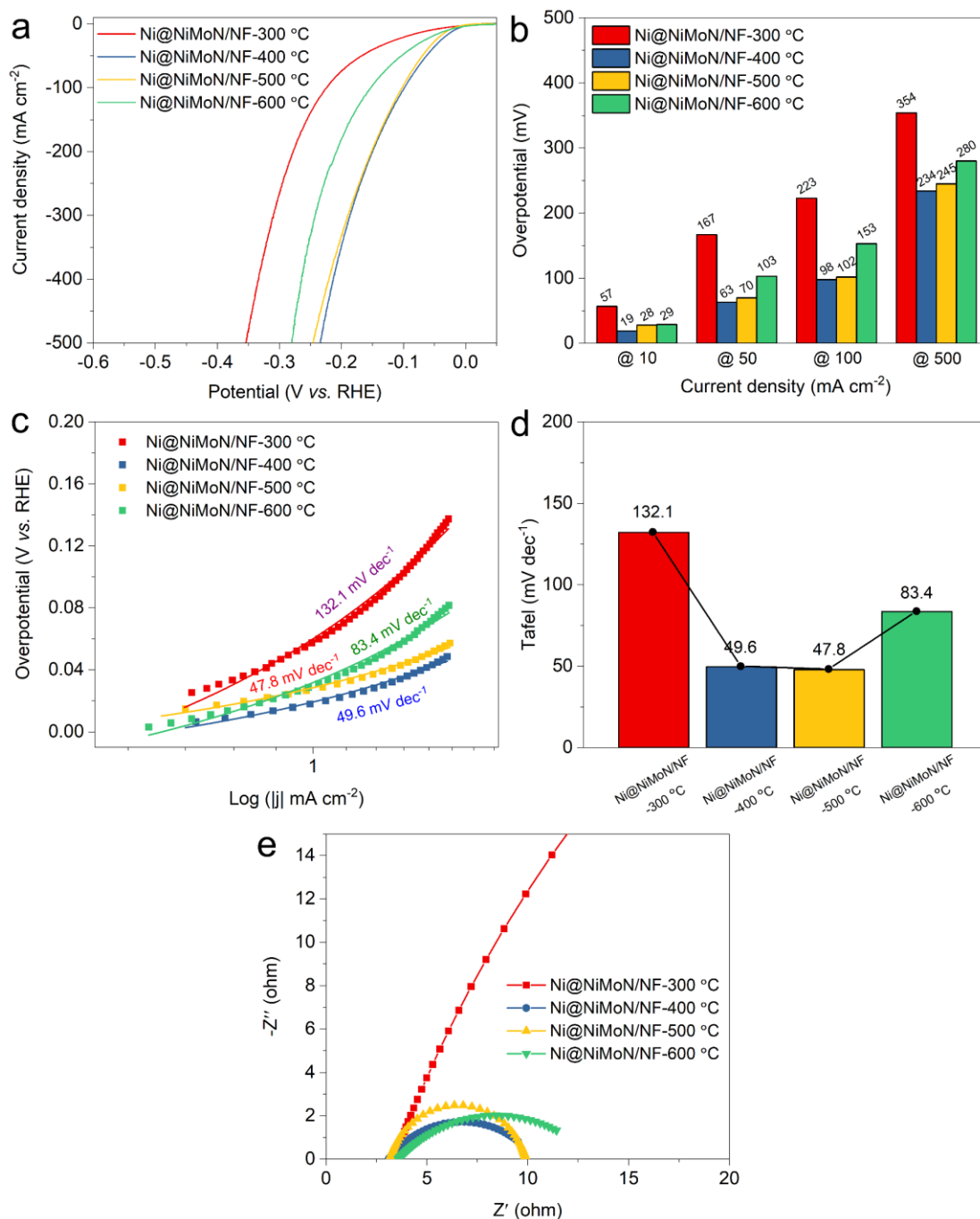
Figure S27. a) LSV curves. c) Tafel plots. e) EIS of Ni@NiMoN/NF catalysts with different pyrolysis temperatures of 300, 400, 500 and 600 °C for HER. Comparison of the (b) overpotentials and (d) Tafel slopes of these catalysts.
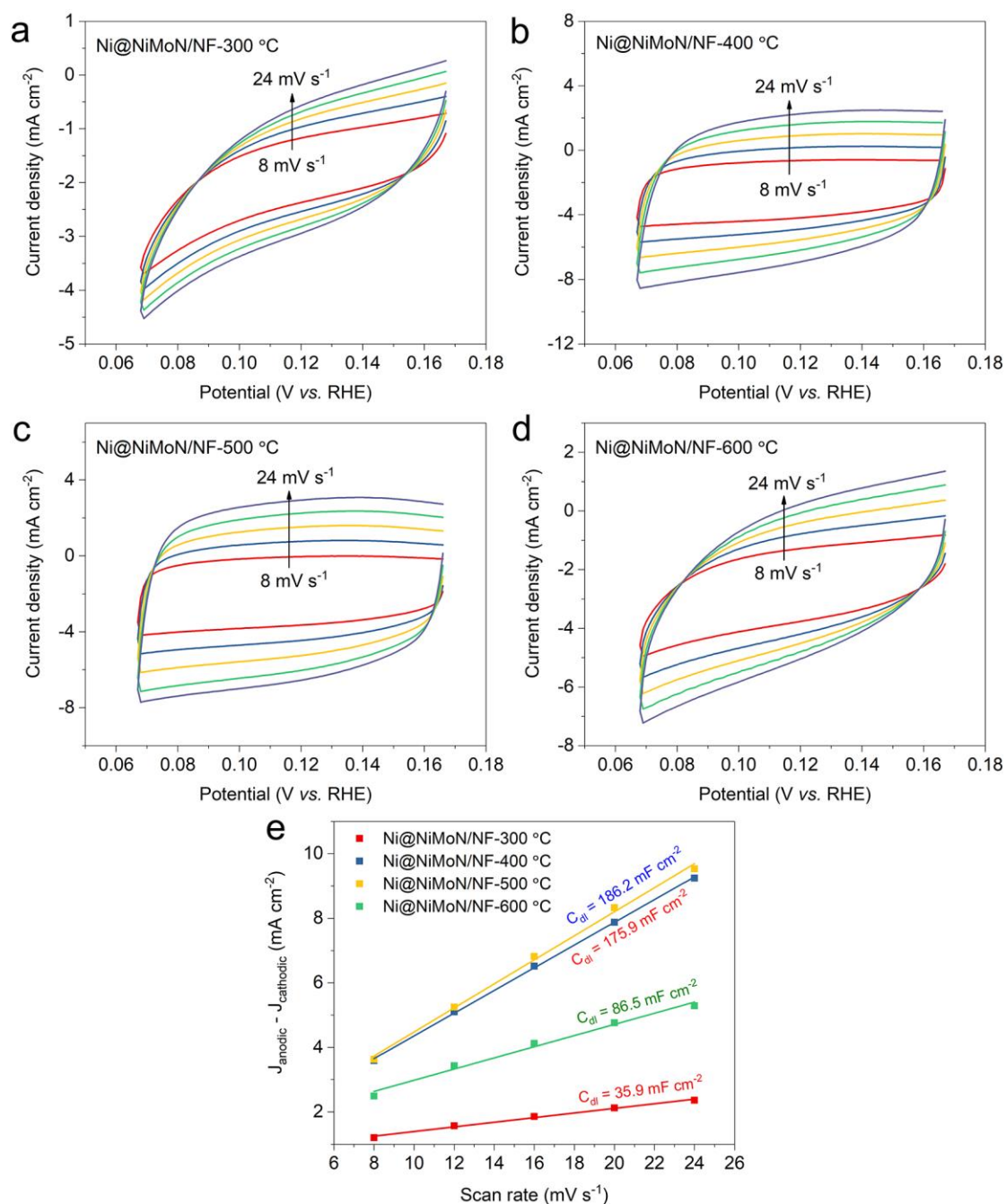
Figure S28. a-d) CV curves of Ni@NiMoN/NF catalysts with different pyrolysis temperatures of 300, 400, 500 and 600 °C at different scan rates in a non-faradaic potential region. e) Corresponding C_{dl} values of these catalysts.

The electrocatalytic HER performances of the prepared catalysts were comprehensively investigated using a traditional three-electrode setup in 1.0 M KOH electrolyte. Generally, the precursor had a decisive effect on the performance of the final catalyst. In order to achieve the optimal catalytic performance of Pt-Ni@NiMoN/NF, we adjusted the catalytic properties of

NiMoO$_4$/NF, Pt-NiMoO$_4$/NF, Ni@NiMoN/NF by controlling the molar ratio of the metal salts (Figure S23 and S24), the concentration of the Pt solution (Figure S25 and S26) and the annealing temperature (Figure S27 and S28), respectively. Based on the results of these pre-experimental tests, for this work, the Pt-Ni@NiMoN/NF catalyst with best HER performance was prepared with the molar ratio of Ni:Mo is 6:7, the Pt solution concentration was 2.0 mg mL^{-1} and the annealing temperature was 400 °C.
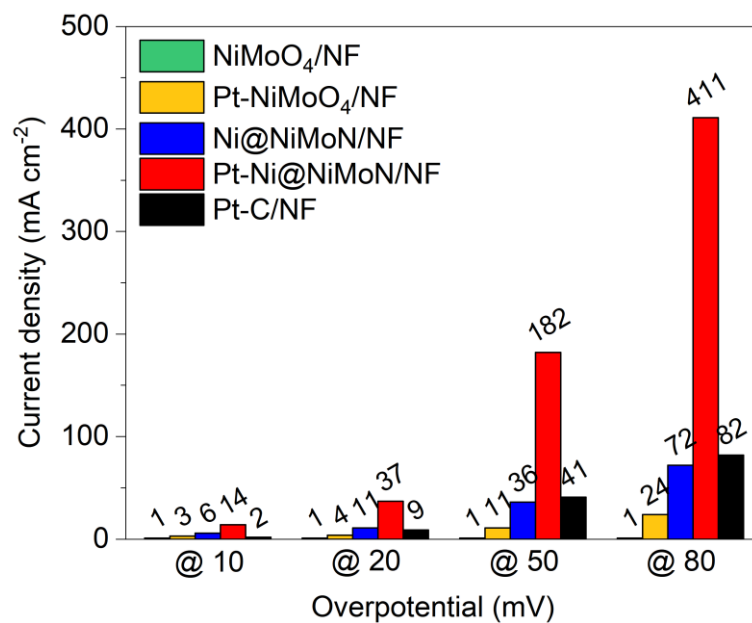
Figure S29. Comparison of the current densities of NiMoO$_4$/NF, Pt-NiMoO$_4$/NF, Ni@NiMoN/NF, Pt-Ni@NiMoN/NF and Pt-C/NF at the overpotentials of 10, 20, 50 and 80 mV.
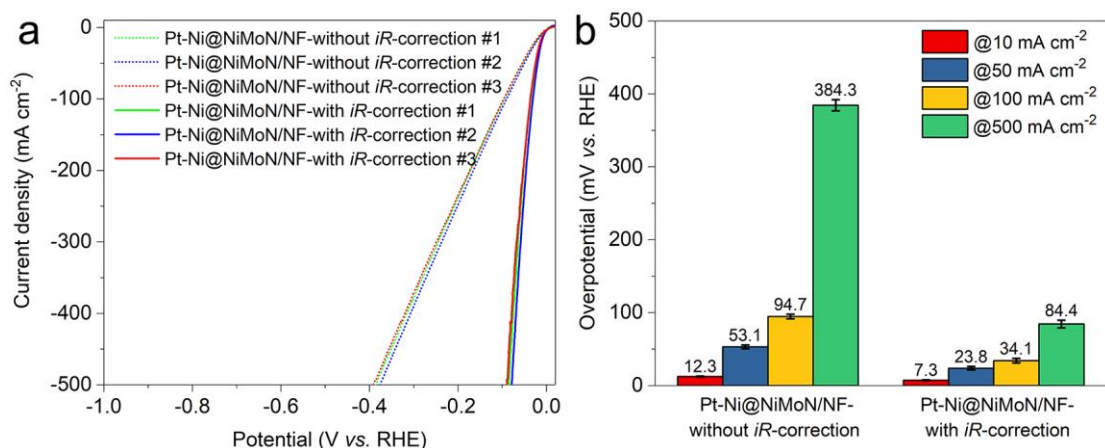
Figure S30. a) LSV curves of Pt-Ni@NiMoN/NF repeatability tests with and without *iR*-correction. b) Comparison of the overpotentials for Pt-Ni@NiMoN/NF with error bars (correspond to standard deviations) at the current densities of 10, 50, 100 and 500 mA cm^{-2}.
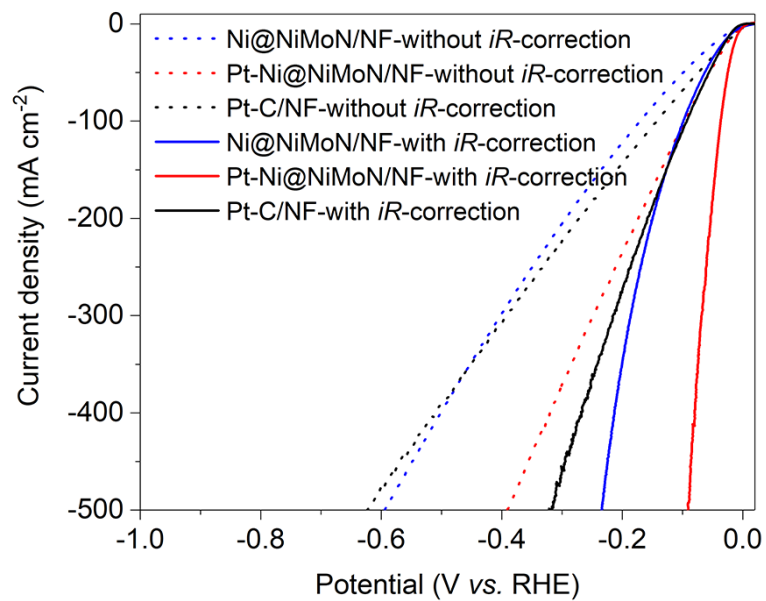
Figure S31. LSV curves of Ni@NiMoN/NF, Pt-Ni@NiMoN/NF and Pt-C/NF with and without *iR*-correction.
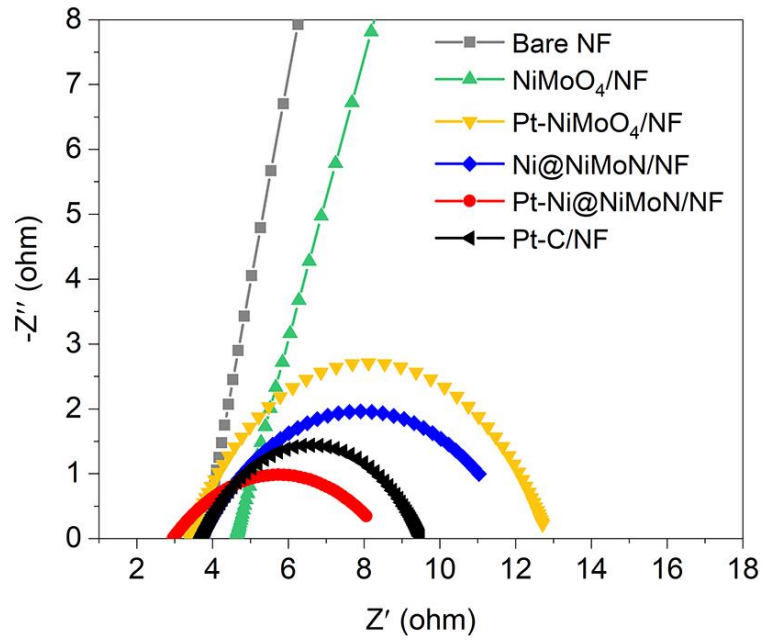
Figure S32. EIS of bare NF, NiMoO$_4$/NF, Pt-NiMoO$_4$/NF, Ni@NiMoN/NF, Pt-Ni@NiMoN/NF and Pt-C/NF catalysts.

Figure S33. CV curves of Bare NF, NiMoO₄/NF, Pt-NiMoO₄/NF, Ni@NiMoN/NF, Pt-Ni@NiMoN/NF and Pt-C/NF catalysts at different scan rates in a non-faradaic potential region.

The current density of the as-prepared catalysts increased with the increase of the scan rates, thereby typically double-layer capacitance characteristics were recorded (Figure S33).

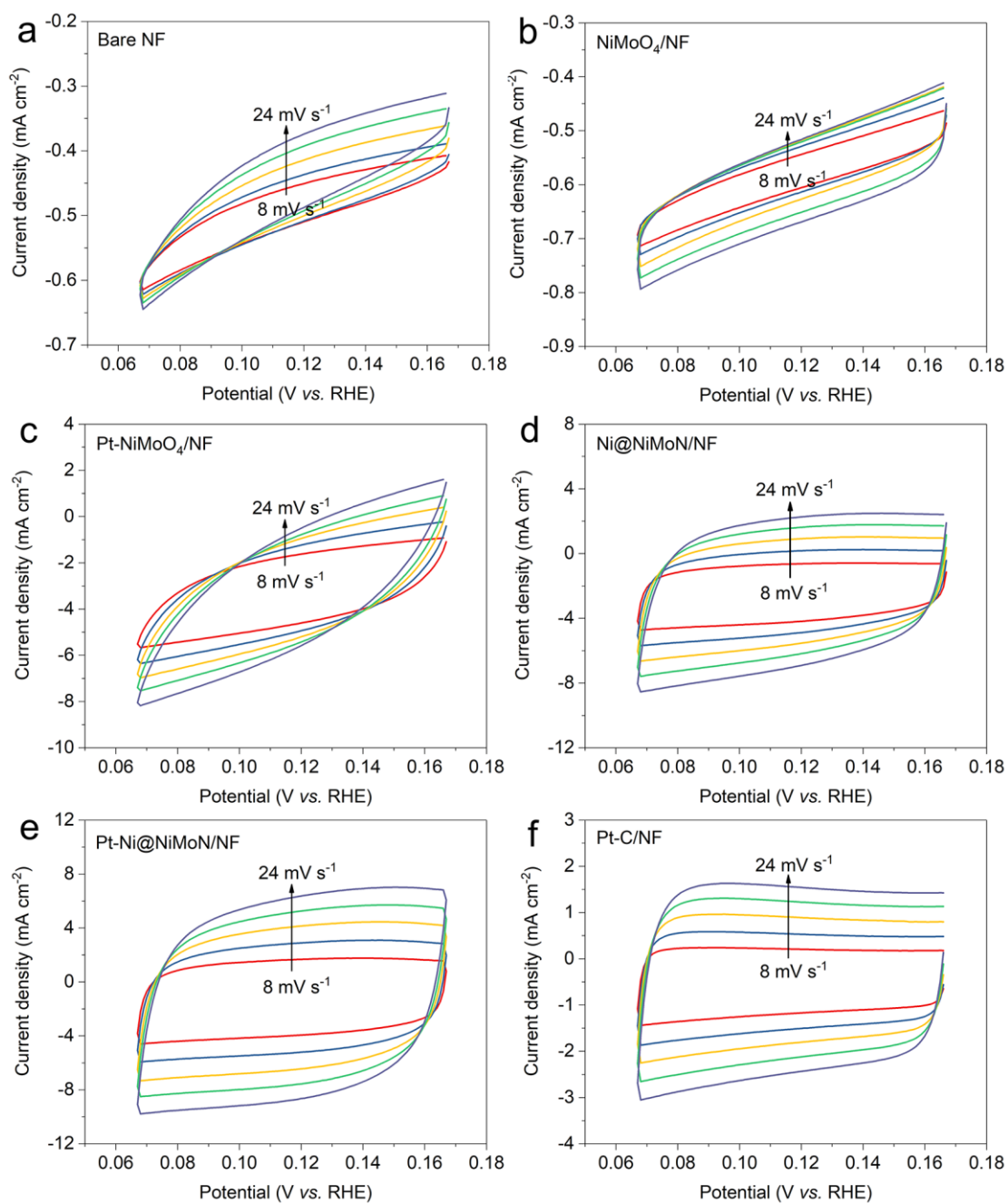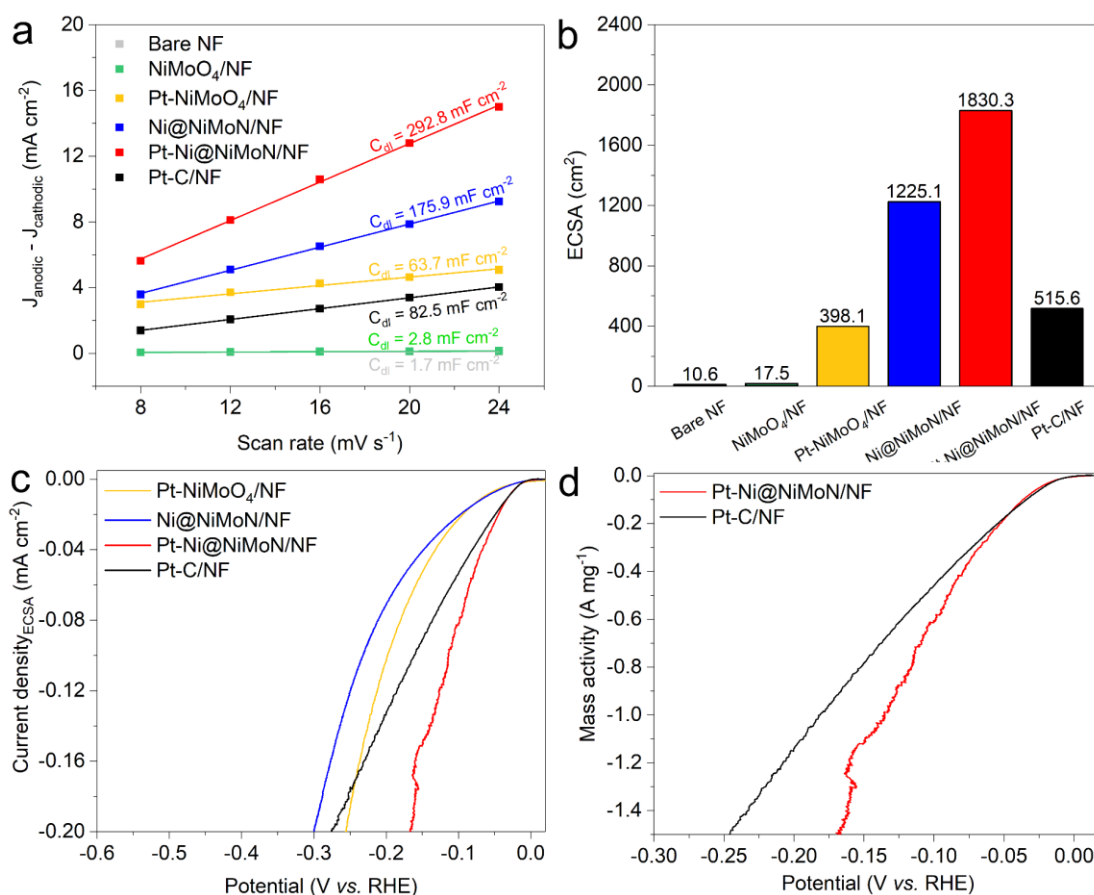**Figure S34.** a) C_{dl}. b) ECSA values of Bare NF, NiMoO$_4$/NF, Pt-NiMoO$_4$/NF, Ni@NiMoN/NF, Pt-Ni@NiMoN/NF and Pt-C/NF catalysts. c) ECSA normalized SA of Pt-NiMoO$_4$/NF, Ni@NiMoN/NF, Pt-Ni@NiMoN/NF and Pt-C/NF catalysts. d) MA normalized by metal mass of Pt-Ni@NiMoN/NF and Pt-C/NF catalysts.

The double-layer capacitances (C_{dl}) were measured to investigate the intrinsic activity sites of catalysts. C_{dl} is proportional to the value of electrochemical active surface areas (ECSA)[18]. The Pt-Ni@NiMoN/NF possessed a higher C_{dl} value (292.8 mF cm^{-2}) when compared to NiMoO$_4$/NF (2.8 mF cm^{-2}), Pt-NiMoO$_4$/NF (63.7 mF cm^{-2}), Ni@NiMoN/NF (196.0 mF cm^{-2}) and (82.5 mF cm^{-2}) (Figure S34a). Correspondingly, the ECSAs were calculated to be 1830.3, 17.5, 398.1, 1225.1 and 515.6 cm^2 (Figure S34b).
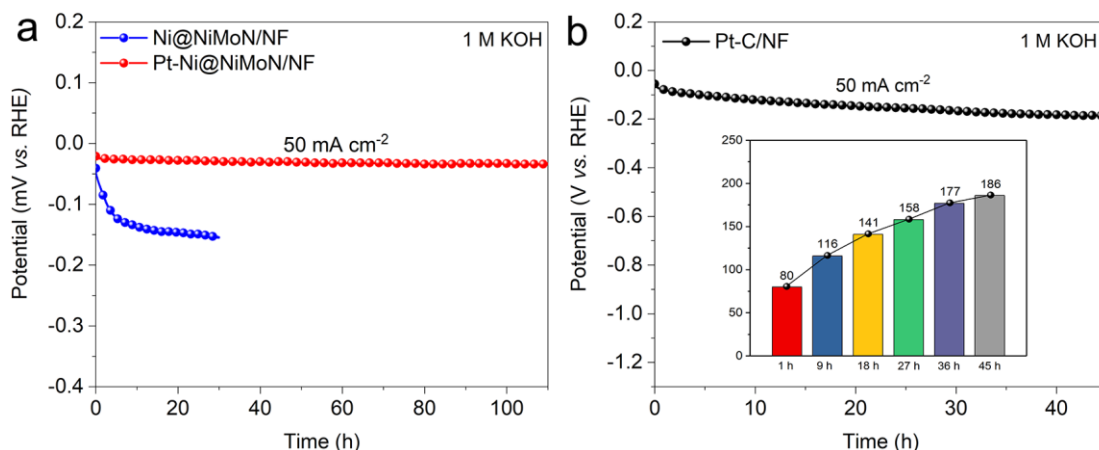
Figure S35. a, b) Chronopotentiometry curves of Ni@NiMoN/NF, Pt-Ni@NiMoN/NF and Pt-C/NF at the current density of 50 mA cm⁻² in 1 M KOH electrolyte (with *iR* correction). Inset: Histogram of the potential of Pt-C/NF at different stability test times.

Figure S35 shows the chronopotentiometry (CP) curves for Pt-Ni@NiMoN/NF, Ni@NiMoN/NF and Pt-C/NF at a current density of 50 mA cm⁻² in 1 M KOH electrolyte. The strong synergistic effect between Pt and NiMoN improves the HER kinetics, optimizing the adsorption energy of intermediate species and preventing the formation of high-energy reactive species that could lead to catalyst degradation. Furthermore, the intrinsic outstanding oxidation and corrosion resistance of Pt significantly contribute to the robustness of the catalyst, effectively enhancing the durability of the catalyst.
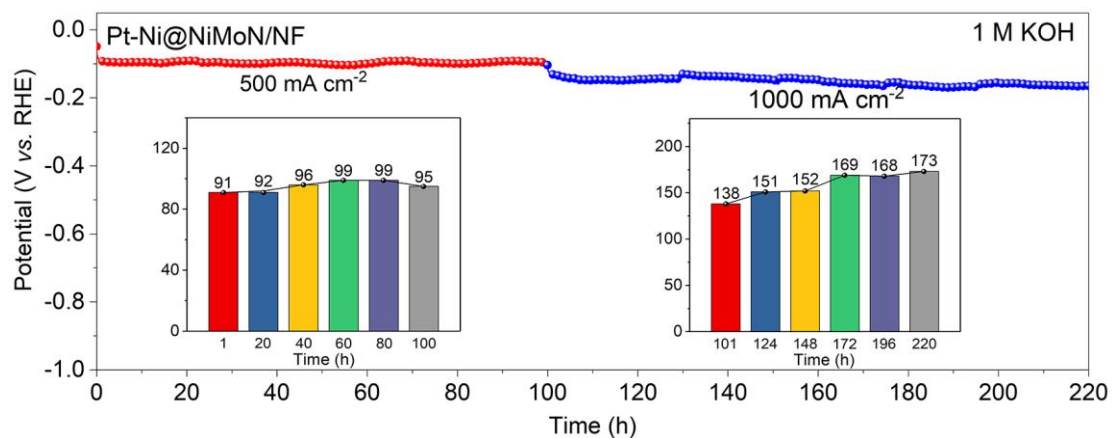
Figure S36. Chronopotentiometry curve of Pt-Ni@NiMoN/NF at the current densities of 500 and 1000 mA cm^{-2} (with *iR* correction). Inset: Histogram of the trend of the overpotential over time.
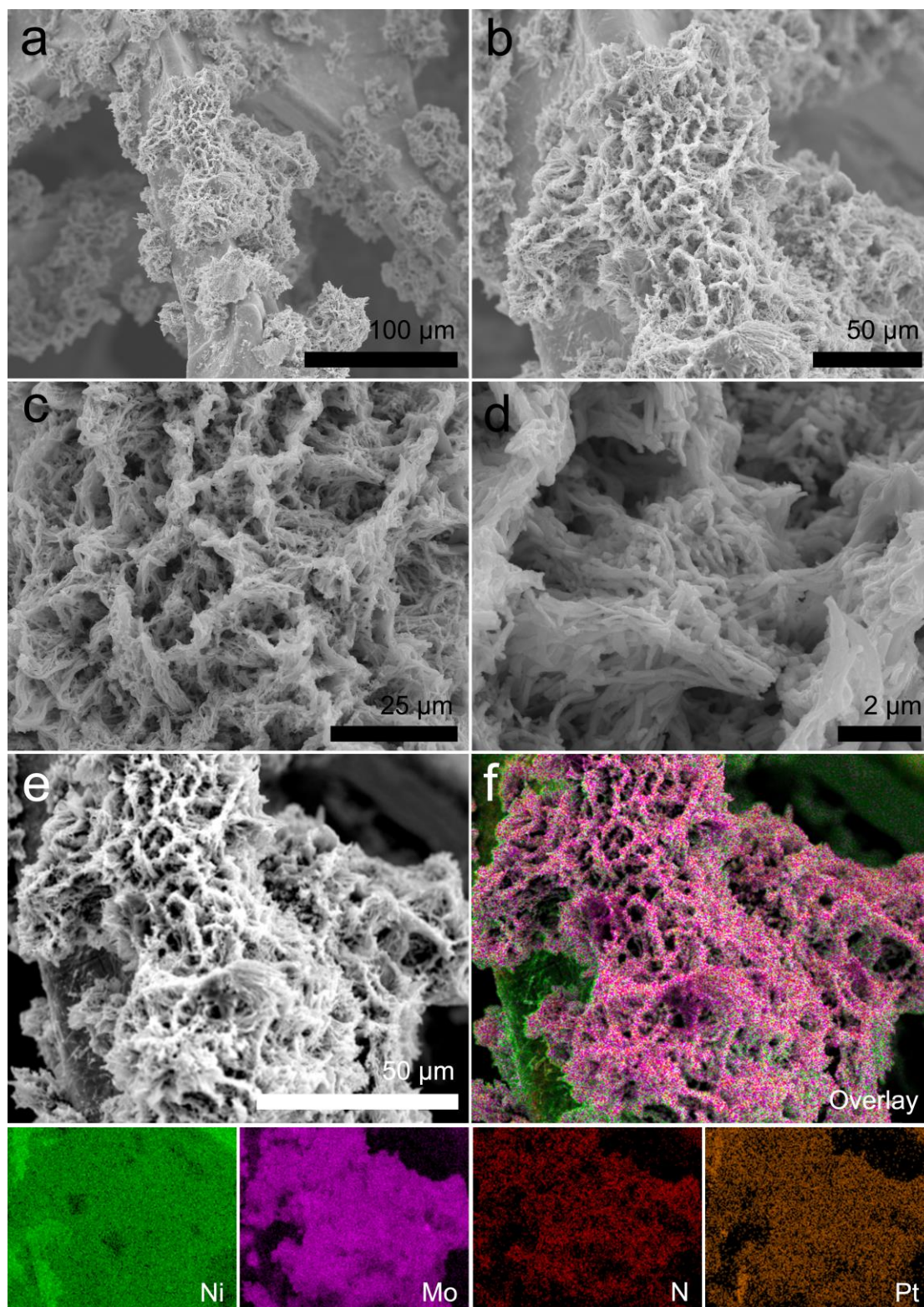
Figure S37. a-e) Low magnification SEM images of Pt-Ni@NiMoN/NF after stability test in 1 M KOH electrolyte. f) EDS elemental mapping of Ni, Mo, N and Pt in Pt-Ni@NiMoN/NF after stability test in 1 M KOH electrolyte.
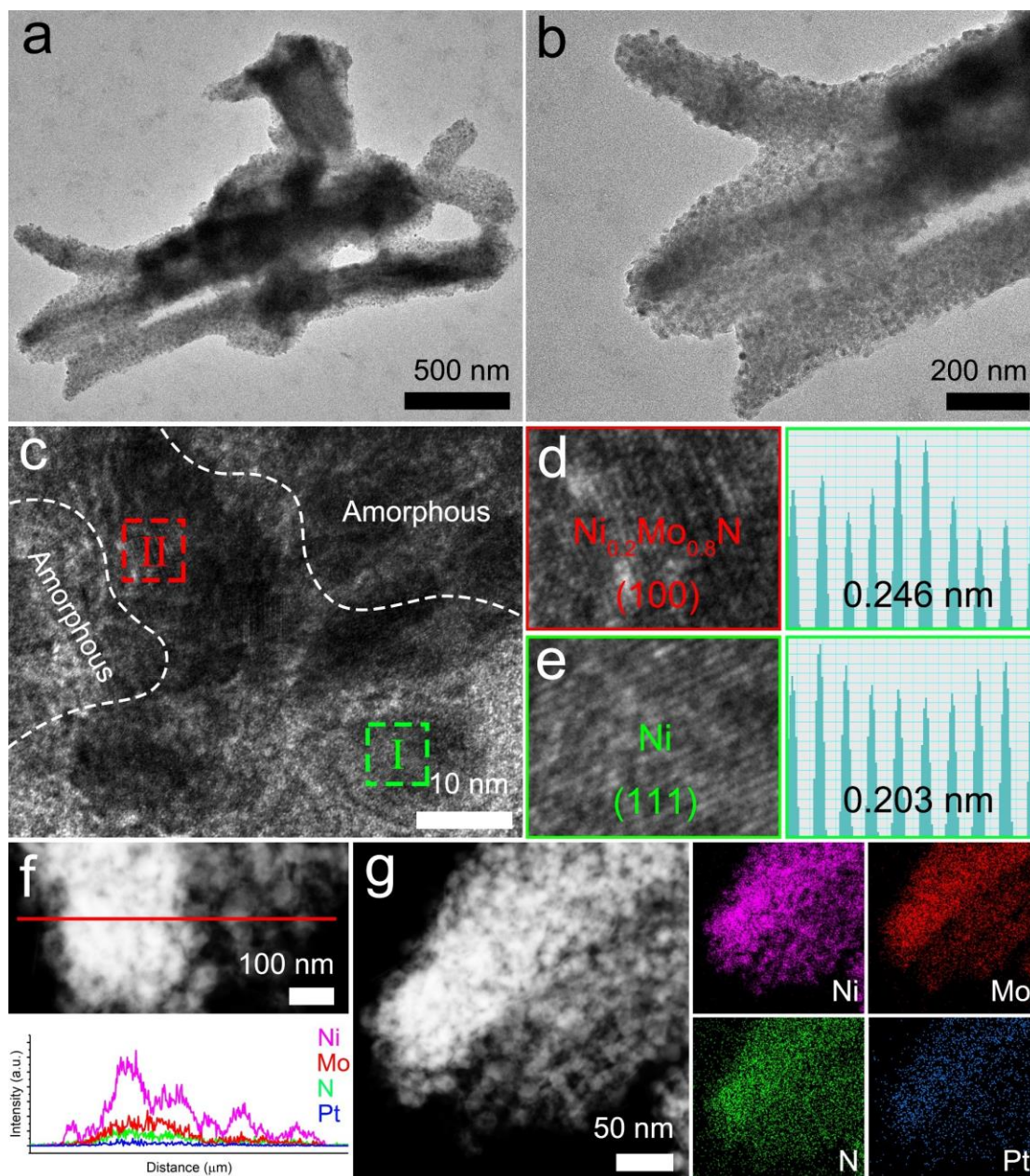
Figure S38. a, b) TEM and c-e) HRTEM images of Pt-Ni@NiMoN/NF after stability test in 1 M KOH electrolyte. Interplanar spacings of the lattice fringes shown in (d-e). f) EDS line scan and corresponding element dispersion. g) HAADF-STEM image and the corresponding EDS elemental mapping of Ni, Mo, N and Pt in Pt-Ni@NiMoN/NF after stability test in 1 M KOH electrolyte.
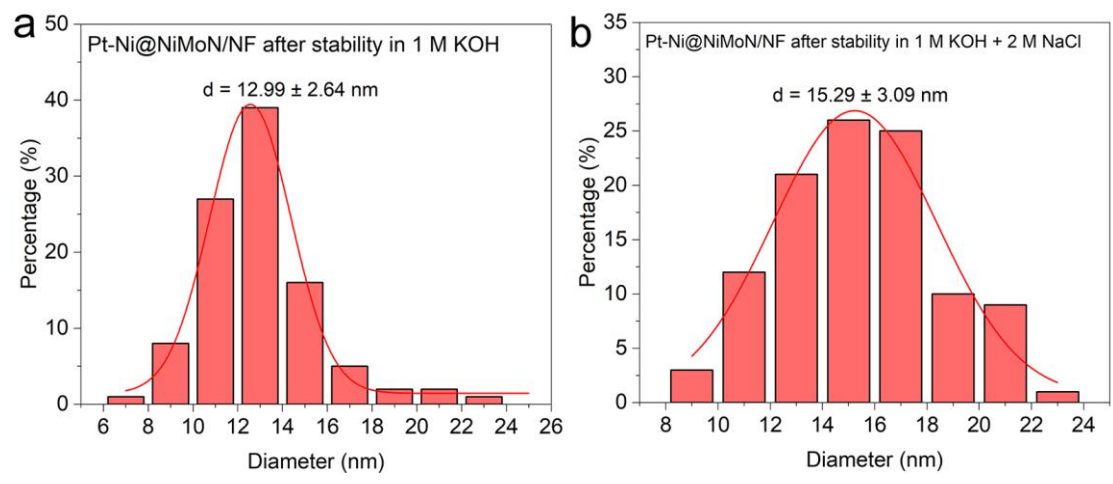
Figure S39. a, b) Diameter distribution of the Ni nanoparticles with Gaussian fit in Pt-Ni@NiMoN/NF after stability in 1 M KOH electrolyte and 1 M KOH + 2 NaCl electrolyte.
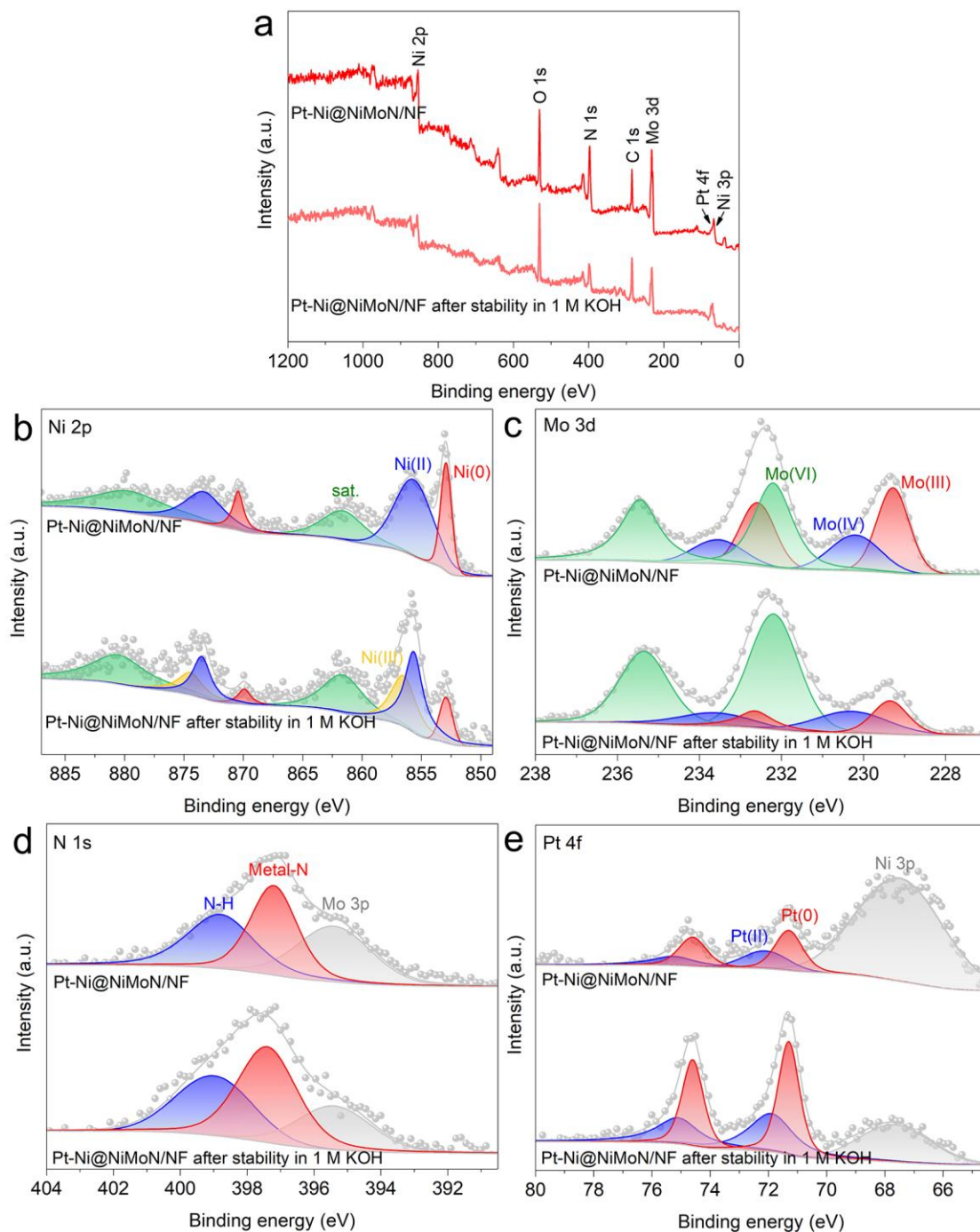
Figure S40. a) Full range XPS spectrum. b-e) High-resolution XPS spectra of Ni 2p, Mo 3d N 1s and Pt 4f of Ni@NiMoN/NF and Pt-Ni@NiMoN/NF after stability in 1 M KOH electrolyte.
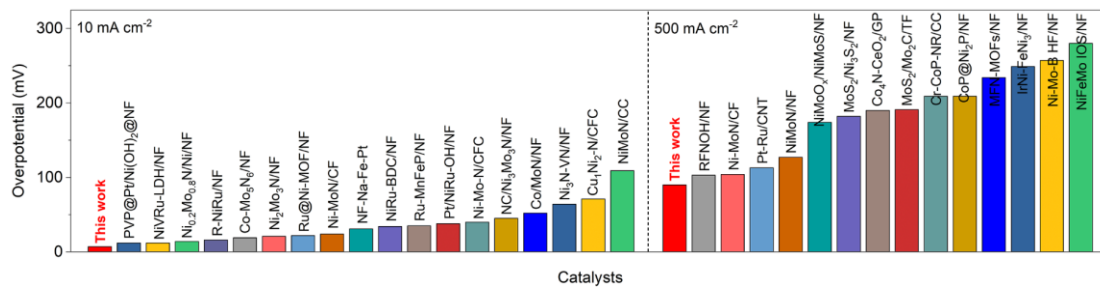
Figure S41. A comparison of the overpotential at the current densities of 10 and 500 mA cm^{-2} for the Pt-Ni@NiMoN/NF with other recently reported self-supported electrocatalysts in 1.0 M KOH solution.
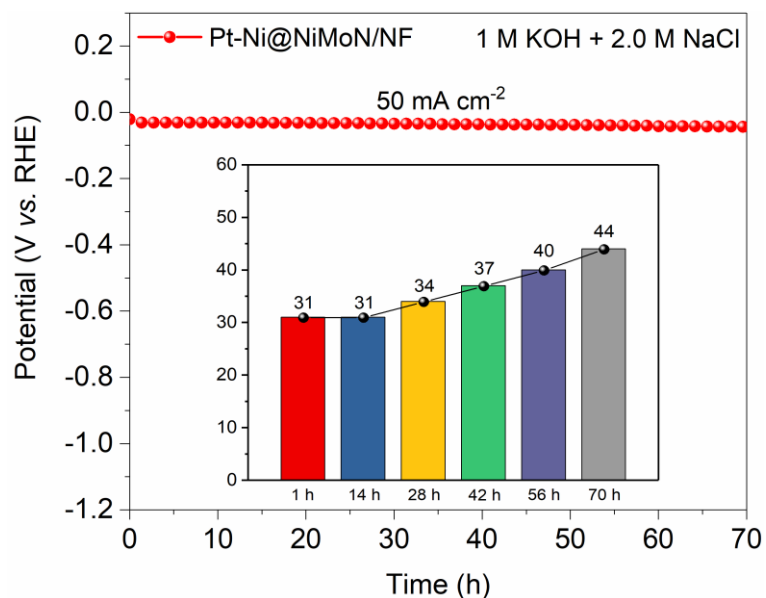
Figure S42. Chronopotentiometry curves of Pt-Ni@NiMoN/NF at the current densities of 50 mA cm^{-2} in 1 M KOH + 2.0 M NaCl electrolyte (with *iR* correction). Inset: Histogram of the potential of Pt-Ni@NiMoN/NF at different stability test times.

Pt-Ni@NiMoN/NF was tested continuously for up to 70 h at the current density of 50 mA cm^{-2} in a harsher environment (1 M KOH + 2.0 M NaCl) (Figure S42).

Figure S43. Optical photographs of the 1 M KOH, 1 M KOH + 0.5 M NaCl and 1 M KOH + seawater electrolytes.
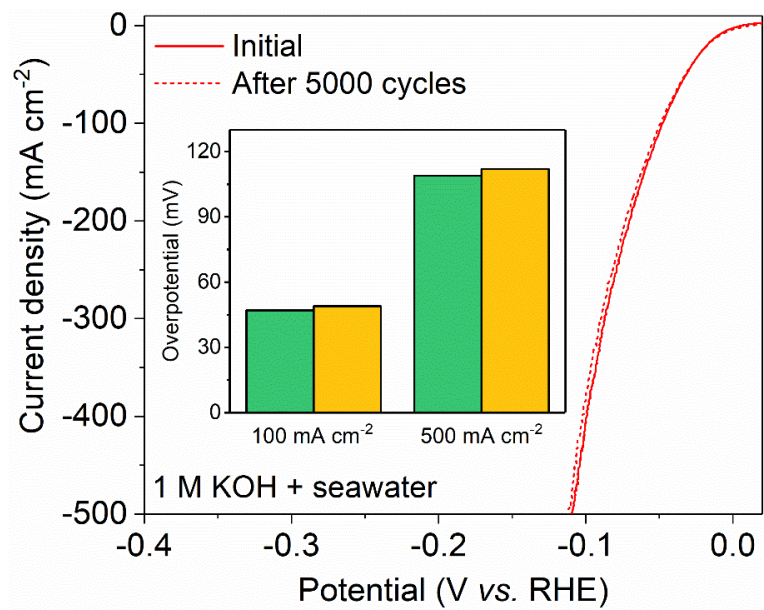
Figure S44. LSV curves of the Pt-Ni@NiMoN/NF before and after 5000 CV.
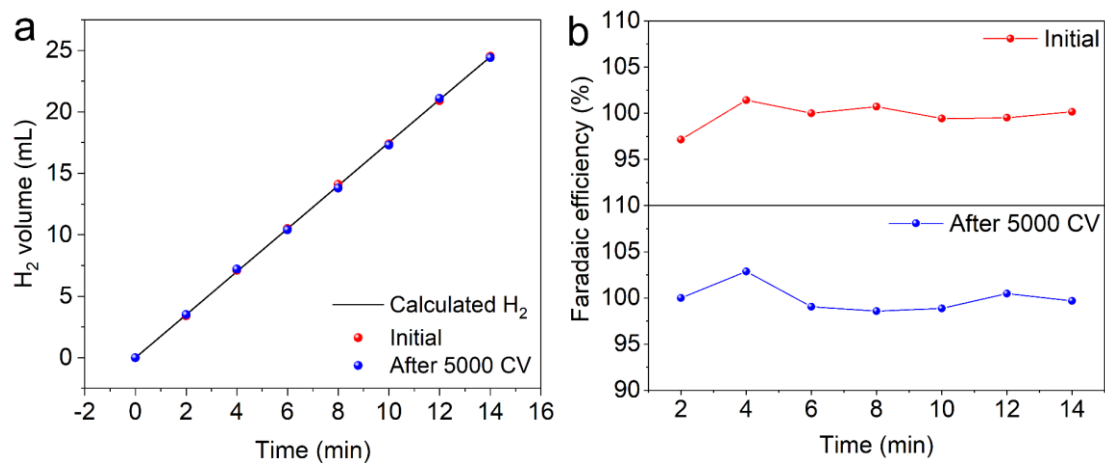
Figure S45. a) Theoretical and actual hydrogen production and b) Faraday efficiency of the Pt-Ni@NiMoN/NF before and after 5000 CV.
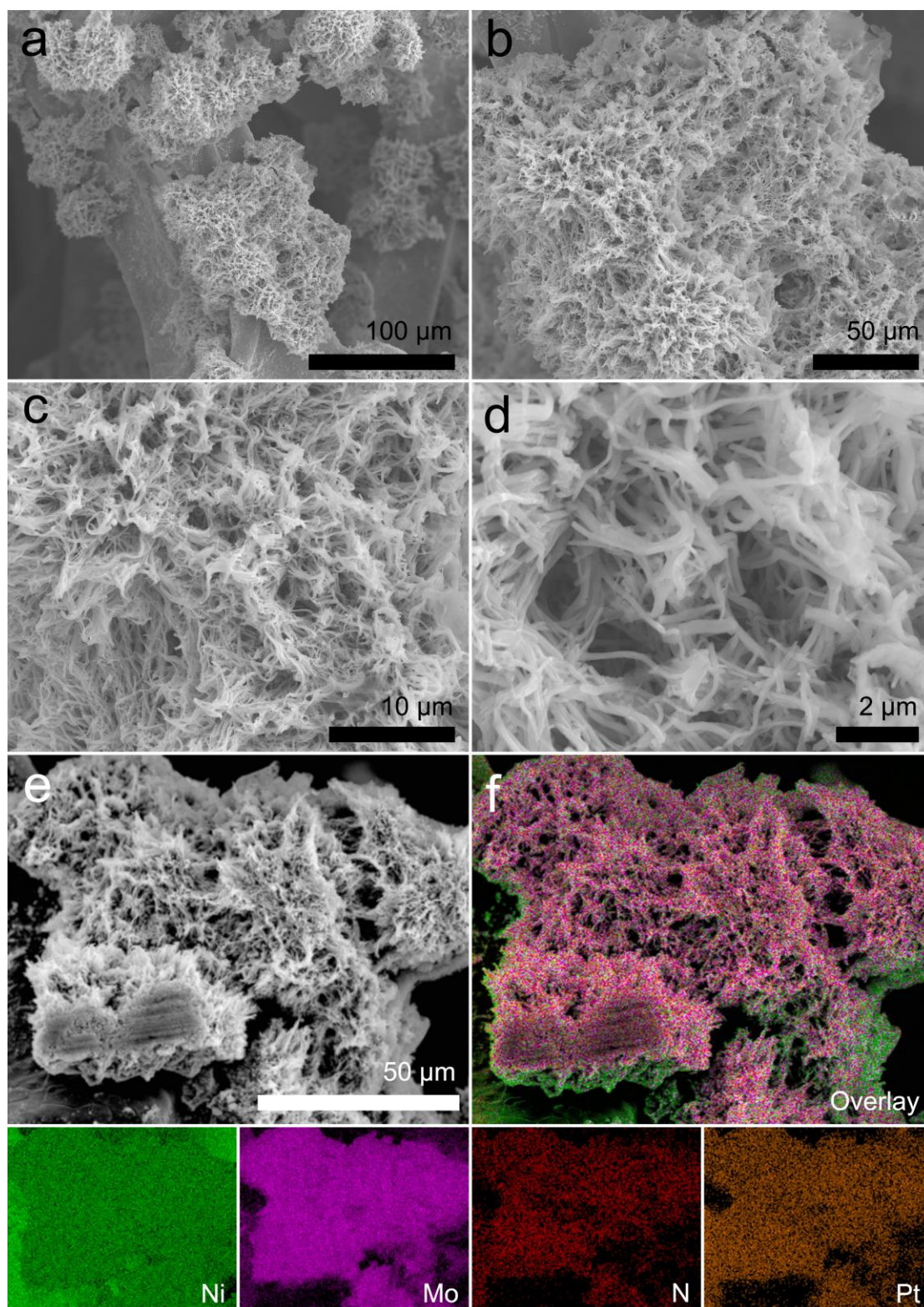
Figure S46. a-e) Low magnification SEM images of Pt-Ni@NiMoN/NF after stability test in 1 M KOH + 2 M NaCl electrolyte. f) EDS elemental mapping of Ni, Mo, N and Pt in Pt-Ni@NiMoN/NF after stability test in 1 M KOH + 2 M NaCl electrolyte.
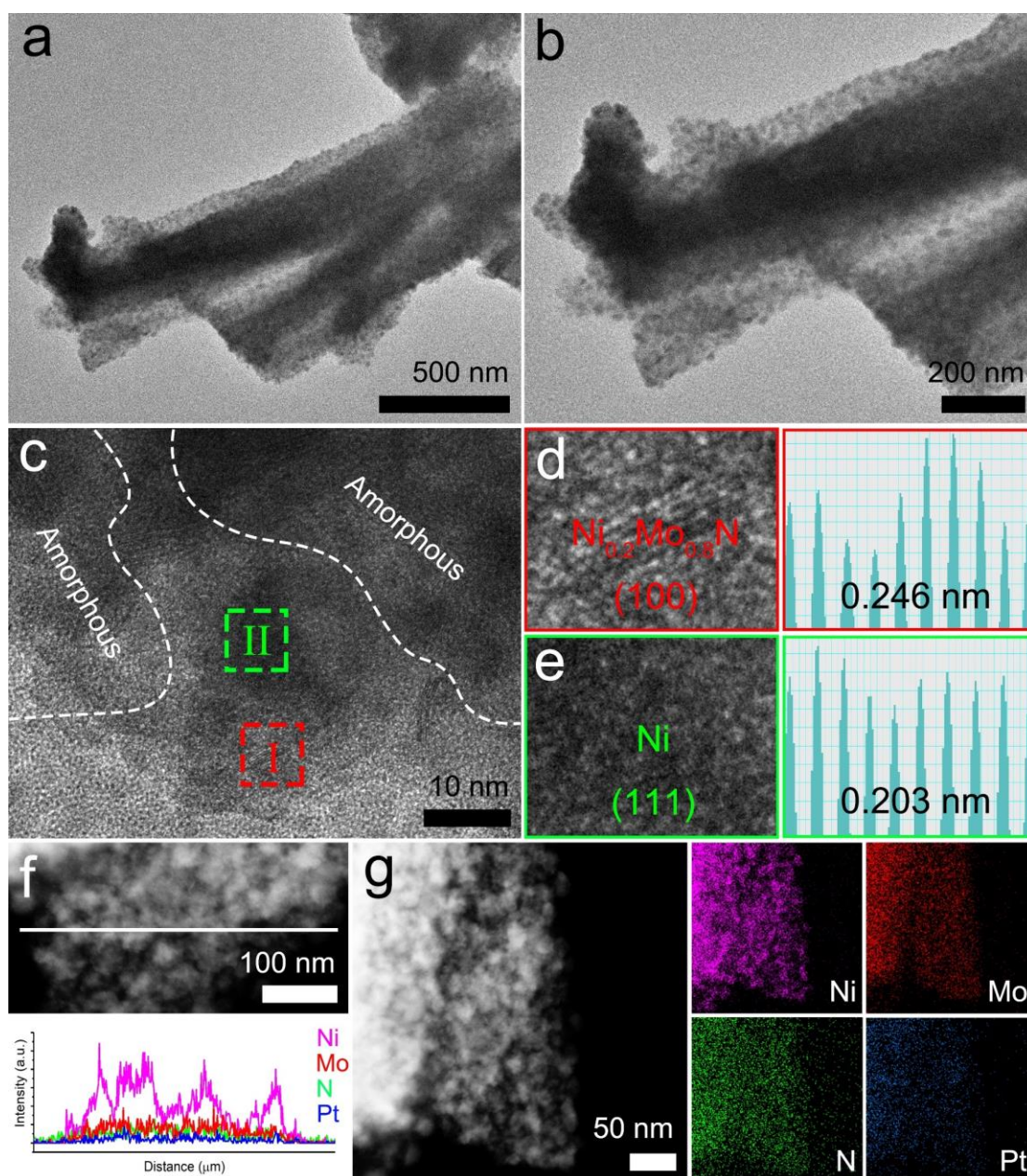
Figure S47. a-b) TEM and c-e) HRTEM images of Pt-Ni@NiMoN/NF after stability test in 1 M KOH + 2 M NaCl electrolyte. Interplanar spacings of the lattice fringes shown in (d-e). f) EDS line scan and corresponding element dispersion. g) HAADF-STEM image and the corresponding EDS elemental mapping of Ni, Mo, N and Pt in Pt-Ni@NiMoN/NF after stability test in 1 M KOH + 2 M NaCl electrolyte.
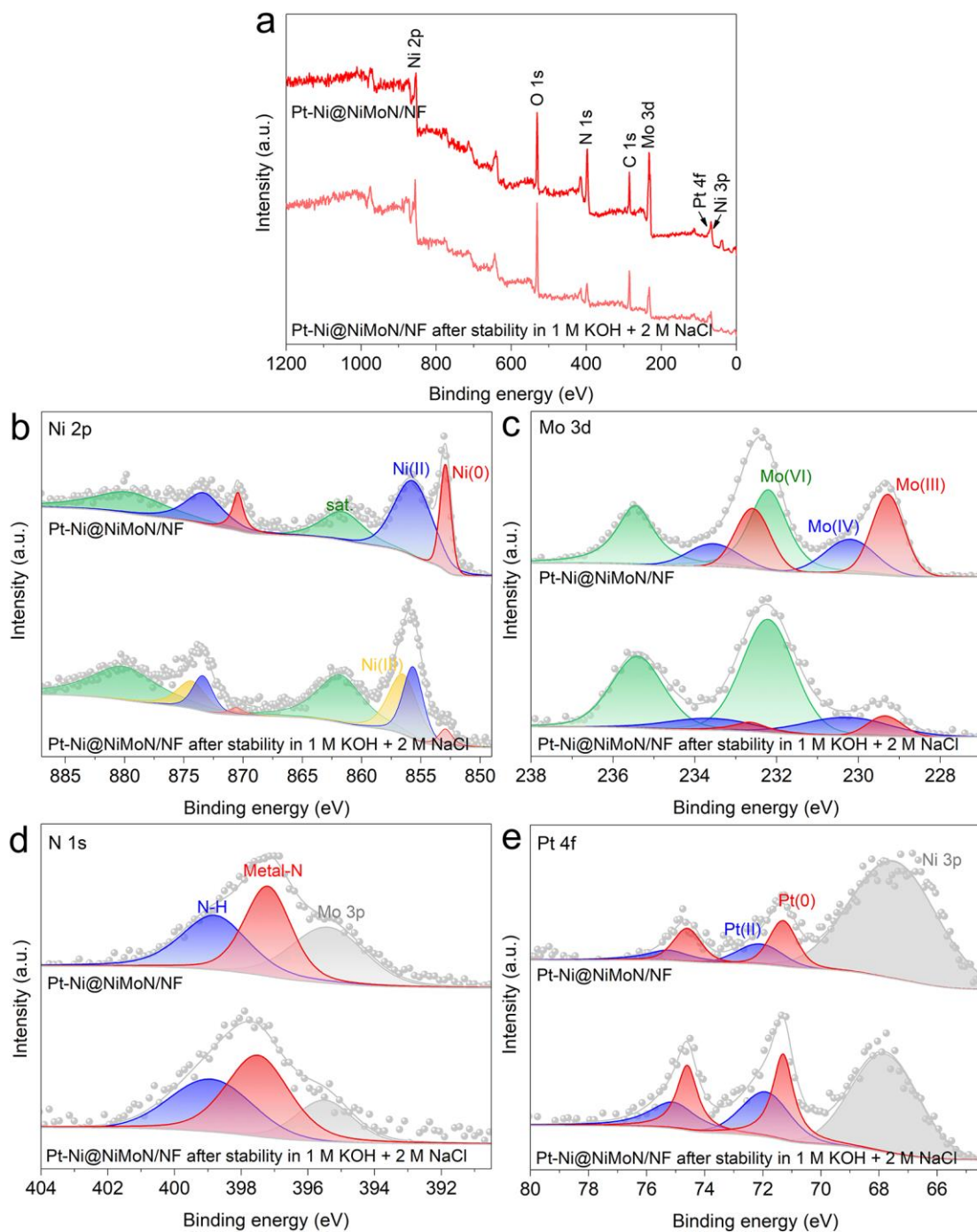
Figure S48. a) Full range XPS spectrum, b) high-resolution XPS spectra of Ni 2p, c) Mo 3d d) N 1s and e) Pt 4f of Ni@NiMoN/NF and Pt-Ni@NiMoN/NF after stability in 1 M KOH + 2 M NaCl electrolyte.

a

Side view

b

Side view

c

Side view

d
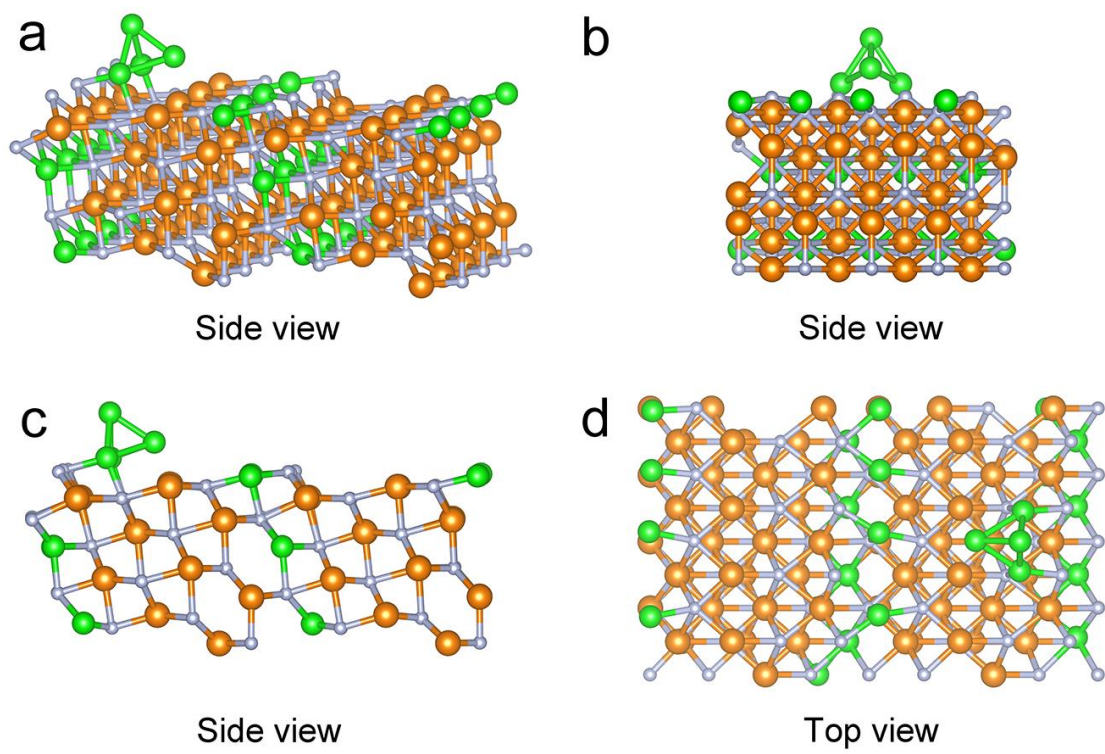
Top view

Figure S49. a-d) Side and top views of the Ni@NiMoN structure models for DFT calculations.

a

Side view

b

Side view

c
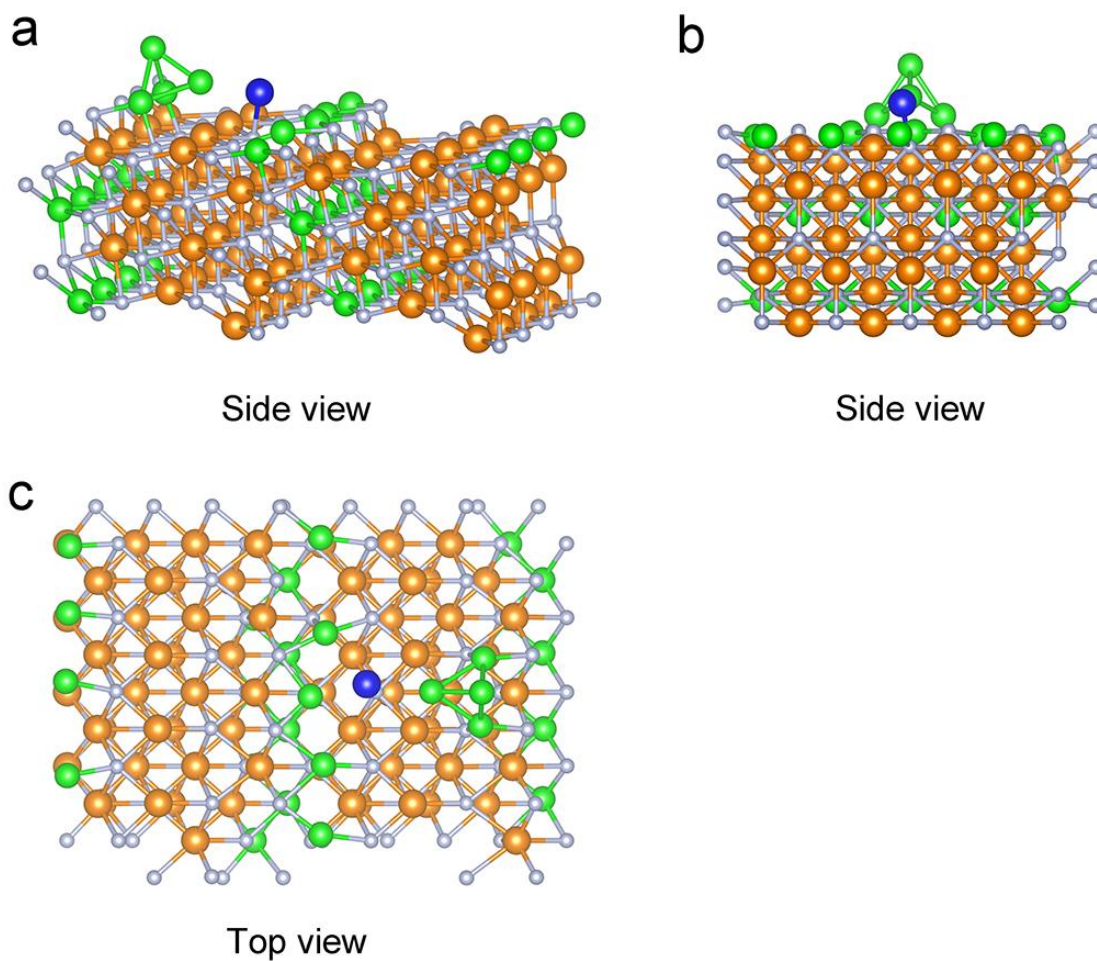
Top view

Figure S50. a-c) Side and top views of the Pt-Ni@NiMoN structure models for DFT calculations.
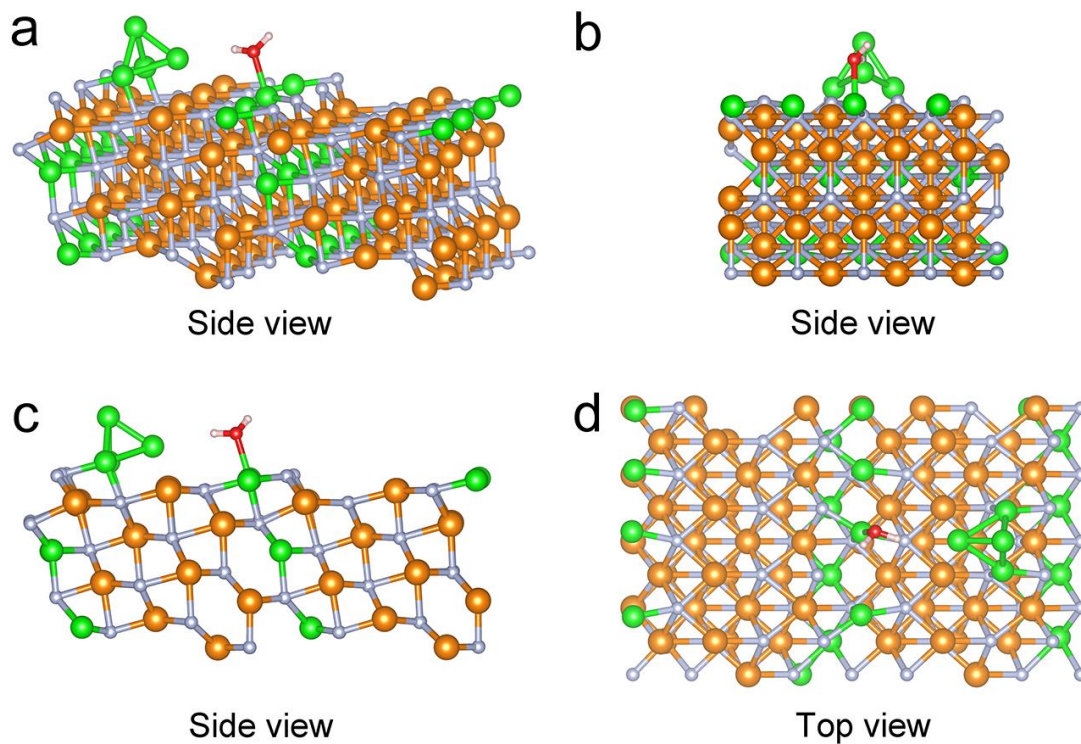
Figure S51. a-d) Side and top views of the structure models for water adsorption in Ni@NiMoN.
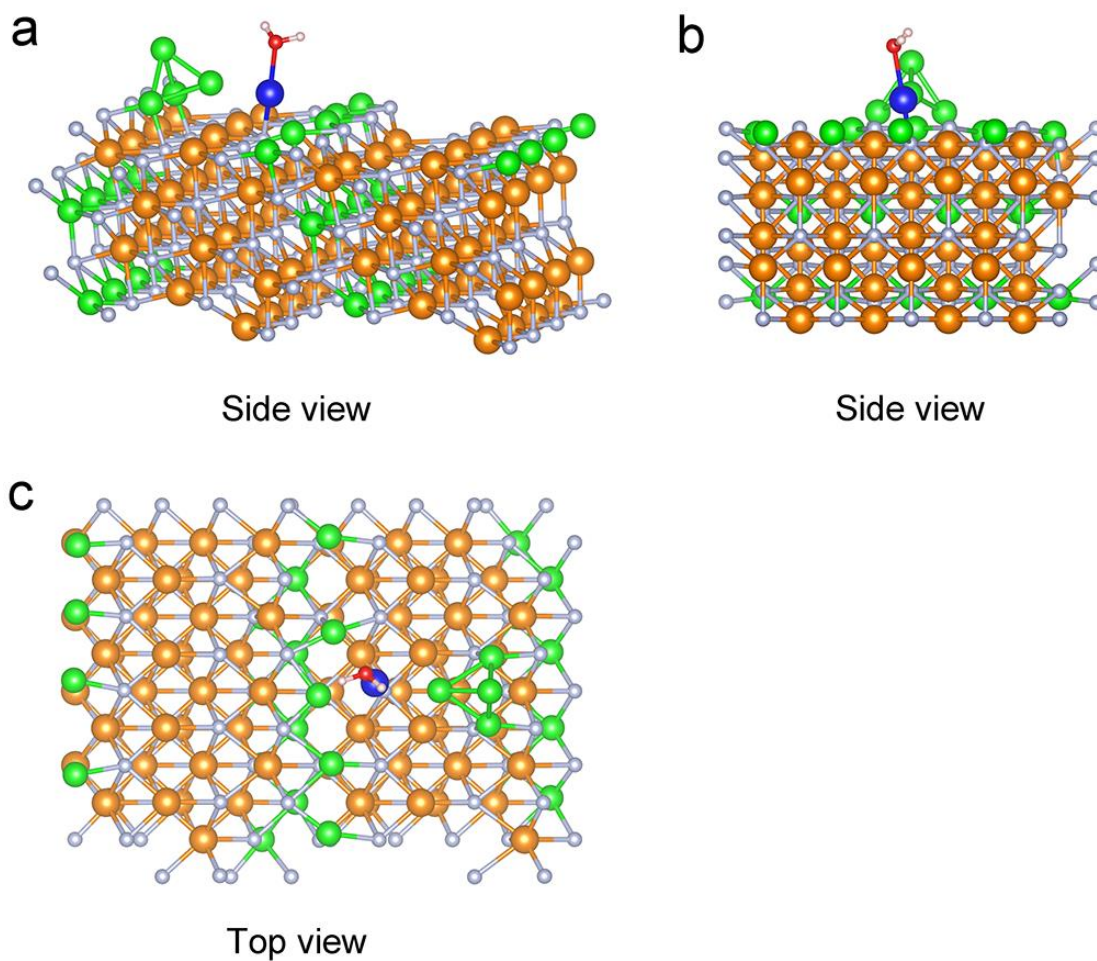
Figure S52. a-c) Side and top views of the structure models for water adsorption in Pt-Ni@NiMoN.
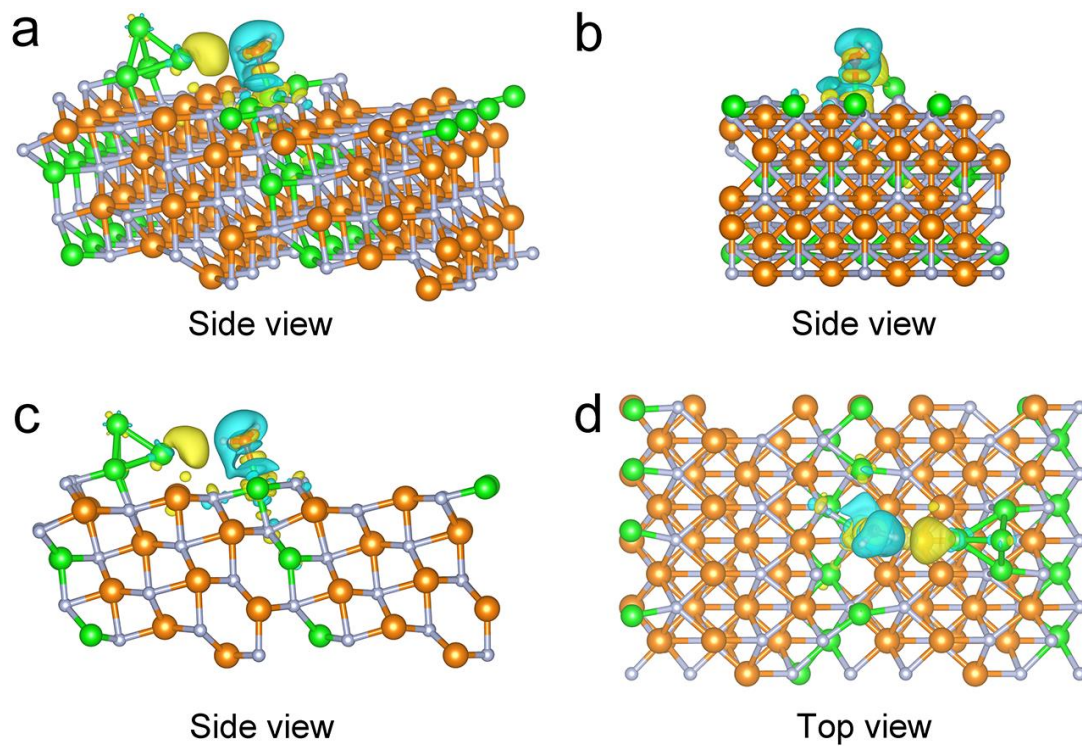
Figure S53. a-d) Side and top views of charge density differences in Ni@NiMoN.
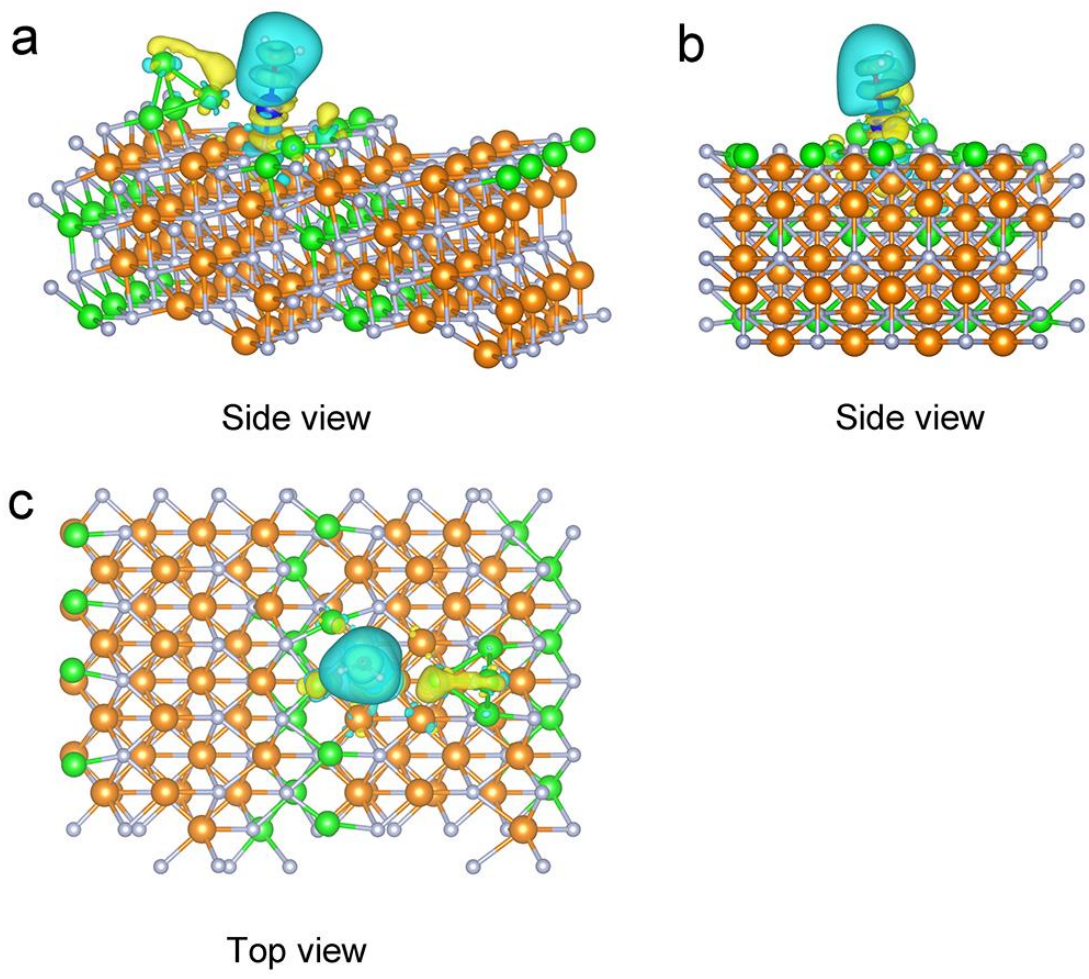
Figure S54. a-c) Side and top views of charge density differences in Pt-Ni@NiMoN.
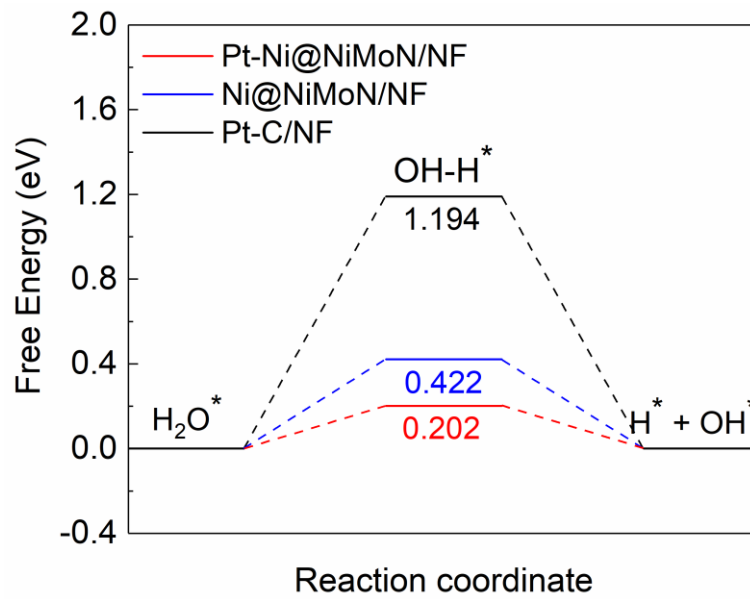
Figure S55. Reaction free energy diagram of H_2O dissociation of Pt-Ni@NiMoN/NF, Ni@NiMoN/NF and Pt-C/NF.

Table S6. Comparison of overpotential (η) at the current density of 10 mA cm^{-2} in 1 M KOH electrolyte between Pt-Ni@NiMoN/NF and recently reported self-supported catalysts.

Catalysts	η@10 mA cm^{-2}	Reference
Pt-Ni@NiMoN/NF	**7 mV**	**This work**
Pt/C/NF	22 mV	This work
PVP@Pt/Ni(OH)$_2$@NF	12 mV	*J. Mater. Chem. A* **9,** 27061-27071 (2021).[19]
NiVRu-LDH/NF	12 mV	*Nat. Commun.* **10,** 3899 (2019).[20]
Ni$_{0.2}$Mo$_{0.8}$N/Ni/NF	14 mV	*Energy Environ. Sci.* **13,** 3007-3013 (2020).[21]
R-NiRu/NF	16 mV	*Adv. Mater.* **33,** e2104764 (2021).[22]
Co-Mo$_5$N$_6$/NF	19 mV	*Adv. Energy Mater.* **10,** 2002176 (2020).[23]
Ni$_2$Mo$_3$N/NF	21 mV	*J. Mater. Chem. A* **9,** 4945-4951 (2021).[17]
Ru@Ni-MOF/NF	22 mV	*Angew. Chem., Int. Ed.* **60,** 22276-22282 (2021).[24]
Ni-MoN/CF	24 mV	*Adv. Mater.* **34,** e2201774 (2022).[8]
NF-Na-Fe-Pt	31 mV	*Appl. Catal., B* **297,** 120395 (2021).[25]
NiRu-BDC/NF	34 mV	*Nat. Commun.* **12,** 1369 (2021).[26]
Ru-MnFeP/NF	35 mV	*Adv. Energy Mater.* **10,** 2000814 (2020).[27]
Pt/NiRu-OH/NF	38 mV	*Appl. Catal., B* **269,** 118824 (2020).[28]
Ni-Mo-N/CFC	40 mV	*Nat. Commun.* **10,** 5335 (2019).[29]
NC/Ni$_3$Mo$_3$N/NF	45 mV	*Appl. Catal., B* **272,** 118956 (2020).[1]
Co/MoN/NF	52 mV	*Appl. Catal., B* **286,** 119882 (2021).[30]
Ni$_3$N-VN/NF	64 mV	*Adv Mater* **31,** e1901174 (2019).[31]
Cu1Ni$_2$-N/CFC	71 mV	*Adv. Energy Mater.* **9,** 1900390 (2019).[32]
NiMoN/CC	109 mV	*Adv. Energy Mater.* **6,** 1600221 (2016).[33]

Table S7. Comparison of overpotential (η) at the current density of 500 mA cm^{-2} in 1 M KOH electrolyte between Pt-Ni@NiMoN/NF and recently reported self-supported catalysts.

Catalysts	η@500 mA cm^{-2}	Reference
Pt-Ni@NiMoN/NF	**90 mV**	**This work**
Pt/C/NF	321 mV	This work
RFNOH/NF	103 mV	*Small Methods* **4,** 1900796 (2020).[34]
Ni-MoN/CF	104 mV	*Adv. Mater.* **34,** e2201774 (2022).[8]
Pt-Ru/CNT	113 mV	*Small* **18,** e2104559 (2022).[35]
NiMoN/NF	127 mV	*Nat. Commun.* **10,** 5106 (2019).[36]
NiMoO$_x$/NiMoS/NF	174 mV	*Nat. Commun.* **11,** 5462 (2020).[37]
MoS$_2$/Ni$_3$S$_2$/NF	182 mV	*Science Bulletin* **65,** 123-130 (2020).[38]
Co$_4$N-CeO$_2$/GP	190 mV	*Adv. Funct. Mater.* **30,** 1910596 (2020).[39]
MoS$_2$/Mo$_2$C/TF	191 mV	*Nat. Commun.* **10,** 269 (2019).[40]
Cr-CoP-NR/CC	209 mV	*Small* **17,** 2100832 (2021).[41]
CoP@Ni$_2$P/NF	209 mV	*Appl. Catal., B* **296,** 120350 (2021).[42]
MFN-MOFs/NF	234 mV	*Nano Energy* **57,** 1-13 (2019).[2]
IrNi-FeNi$_3$/NF	249 mV	*Appl. Catal., B* **286,** 119881 (2021).[43]
Ni-Mo-B HF/NF	257 mV	*Adv. Funct. Mater.* **32,** 2107308 (2021).[44]
NiFeMo IOS/NF	280 mV	*Adv. Energy Mater.* **7,** 1601390 (2017).[45]

Table S8. Comparison of overpotential (η) at the current density of 10 mA cm^{-2} in 1 M KOH + real seawater electrolyte between Pt-Ni@NiMoN/NF and recently reported self-supported catalysts.

Catalysts	η@10 mA cm^{-2}	Reference
Pt-Ni@NiMoN/NF	**11 mV**	**This work**
Pt/C/NF	24 mV	This work
CeO$_2$/α-MoC/β-Mo$_2$C MRs/CC	29 mV	*Appl. Catal., B* **317**, 121774 (2022).[46]
Fe$_{0.01}$-Ni&Ni$_{0.2}$Mo$_{0.8}$N	33 mV	*Energy Environ. Sci.* **15**, 3945-3957 (2022).[47]
Ni$_3$N/W$_5$N$_4$	36 mV	*Appl. Catal., B* **307**, 121198 (2022).[48]
Ni/β-Ni(OH)$_2$ NSAs	62 mV	*J. Mater. Chem. A*, 21848-21855 (2022).[49]
NiCoHPi@Ni$_3$N/NF	87 mV	*ACS Appl. Mater. Interfaces* **14**, 22061-22070 (2022).[50]
Ni$_2$P-Fe$_2$P/NF	220 mV	*Adv. Funct. Mater.* **31**, 2006484 (2020).[51]

Table S9. Comparison of overpotential (η) at the current density of 100 mA cm^{-2} in 1 M KOH + real seawater electrolyte between Pt-Ni@NiMoN/NF and recently reported self-supported catalysts.

Catalysts	η@100 mA cm^{-2}	Reference
Pt-Ni@NiMoN/NF	**47 mV**	**This work**
Pt/C/NF	109 mV	This work
NiMoN/NF	82 mV	*Nat. Commun.* **10**, 5106 (2019).[36]
Fe$_{0.01}$-Ni&Ni$_{0.2}$Mo$_{0.8}$N	100 mV	*Energy Environ. Sci.* **15**, 3945-3957 (2022).[47]
Ni$_3$N@C/NF	142 mV	*J. Mater. Chem. A* **9**, 13562-13569 (2021).[52]
NiCoHPi@Ni$_3$N/NF	182 mV	*ACS Appl. Mater. Interfaces* **14**, 22061-22070 (2022).[50]
S,P-(Ni,Mo,Fe)OOH/NiMoP/wood aerogel	212 mV	*Appl. Catal., B* **293**, 120215 (2021).[53]
NiPS/NF	329 mV	*J. Energy Chem.* **75**, 66-73 (2022).[54]

Table S10. Comparison of overpotential (η) at the current density of 500 mA cm^{-2} in 1 M KOH + real seawater electrolyte between Pt-Ni@NiMoN/NF and recently reported self-supported catalysts.

Catalysts	η@500 mA cm^{-2}	Reference
Pt-Ni@NiMoN/NF	**109 mV**	**This work**
Pt/C/NF	354 mV	This work
Fe$_{0.01}$-Ni&Ni$_{0.2}$Mo$_{0.8}$N	144 mV	*Energy Environ. Sci.* **15**, 3945-3957 (2022).[47]
NiMoN/NF	160 mV	*Nat. Commun.* **10**, 5106 (2019).[36]
S,P-(Ni,Mo,Fe)OOH/NiMoP/wood aerogel	258 mV	*Appl. Catal., B* **293**, 120215 (2021).[53]
Fe-CoNiP@NC	260 mV	*Chem. Eng. J.* **446**, 136987 (2022).[55]
CoO@C/MXene/NF	270 mV	*Adv. Mater.* **34**, e2109321 (2022).[56]
NiCo@C/MXene/CF	275 mV	*Nat. Commun.* **12**, 4182 (2021).[57]
Ru-FeP$_4$/IF	275 mV	*Appl. Catal., B* **319**, 121950 (2022).[58]
Ni$_3$N@C/NF	279 mV	*J. Mater. Chem. A* **9**, 13562-13569 (2021).[52]
NiCoHPi@Ni$_3$N/NF	281 mV	*ACS Appl. Mater. Interfaces* **14**, 22061-22070 (2022).[50]
RuNi‐Fe$_2$O$_3$/IF	300 mV	*Chin. J. Catal.* **43**, 2202-2211 (2022).[59]
Ni$_2$P-Fe$_2$P/NF	340 mV	*Adv. Funct. Mater.* **31**, 2006484 (2020).[51]
NiPS/NF	391 mV	*J. Energy Chem.* **75**, 66-73 (2022).[54]

Caption for Video S1: The hydrogen evolution from seawater.

Reference

1.   Y. Chen, J. Yu, J. Jia, F. Liu, Y. Zhang, G. Xiong, R. Zhang, R. Yang, D. Sun, H. Liu and W. Zhou, *Appl. Catal., B*, 2020, **272**, 118956.

2.   D. S. Raja, H. W. Lin and S. Y. Lu, *Nano Energy*, 2019, **57**, 1-13.

3.   W. Zheng, *ACS Energy Lett.*, 2023, **8**, 1952-1958.

4.   S. Sun, G. Sun, P. Cheng, R. Liu and C. Zhang, *Mater. Today Energy*, 2023, **32**, 101246.

5.   S. Anantharaj and S. Noda, *J. Mater. Chem. A*, 2022, **10**, 9348-9354.

6.   A. R. Heenan, J. Hamonnet and A. T. Marshall, *ACS Energy Lett.*, 2022, **7**, 2357-2361.

7.   H. Guo, A. Wu, Y. Xie, H. Yan, D. Wang, L. Wang and C. Tian, *J. Mater. Chem. A*, 2021, **9**, 8620-8629.

8.   L. Wu, F. Zhang, S. Song, M. Ning, Q. Zhu, J. Zhou, G. Gao, Z. Chen, Q. Zhou, X. Xing, T. Tong, Y. Yao, J. Bao, L. Yu, S. Chen and Z. Ren, *Adv. Mater.*, 2022, **34**, e2201774.

9.   A. Vadakkayil, C. Clever, K. N. Kunzler, S. Tan, B. P. Bloom and D. H. Waldeck, *Nat. Commun.*, 2023, **14**, 1067.

10.   S. Hou, W. Li, S. Watzele, R. M. Kluge, S. Xue, S. Yin, X. Jiang, M. Döblinger, A. Welle, B. Garlyyev, M. Koch, P. Müller-Buschbaum, C. Wöll, A. S. Bandarenka and R. A. Fischer, *Adv. Mater.*, 2021, **33**, 2103218.

11.   G. Kresse and J. Furthmüller, *Phys. Rev. B*, 1996, **54**, 11169-11186.

12.   G. Kresse and J. Furthmüller, *Comput. Mater. Sci.*, 1996, **6**, 15-50.

13.   John P. Perdew, Kieron Burke and M. Ernzerhof, *Phys. Rev. Lett.*, 1996, **77**, 3865-3868.

14.   H. J. Monkhorst and J. D. Pack, *Phys. Rev. B*, 1976, **13**, 5188-5192.

15.   S. Grimme, *J. Comput. Chem.*, 2006, **27**, 1787-1799.

16.   B. Wang, L. Guo, J. Zhang, Y. Qiao, M. He, Q. Jiang, Y. Zhao, X. Shi and F. Zhang, *Small*, 2022, **18**, e2201927.

17.   S. H. Park, T. H. Jo, M. H. Lee, K. Kawashima, C. B. Mullins, H. K. Lim and D. H. Youn, *J. Mater. Chem. A*, 2021, **9**, 4945-4951.

18.   S. Li, Z. Zhao, T. Ma, P. Pachfule and A. Thomas, *Angew. Chem., Int. Ed.*, 2022, **61**, e202112298.

19.   J. Li, B. Li, H. Huang, S. Yan, C. Yuan, N. Wu, D. Guo and X. Liu, *J. Mater. Chem. A*, 2021, **9**, 27061-27071.

20.   D. Wang, Q. Li, C. Han, Q. Lu, Z. Xing and X. Yang, *Nat. Commun.*, 2019, **10**, 3899.

21.   B. Zhang, L. Zhang, Q. Tan, J. Wang, J. Liu, H. Wan, L. Miao and J. Jiang, *Energy Environ. Sci.*, 2020, **13**, 3007-3013.

22.   X. Chen, J. Wan, J. Wang, Q. Zhang, L. Gu, L. Zheng, N. Wang and R. Yu, *Adv. Mater.*, 2021, **33**, e2104764.

23.   F. Lin, Z. Dong, Y. Yao, L. Yang, F. Fang and L. Jiao, *Adv. Energy Mater.*, 2020, **10**, 2002176.

24.   L. Deng, F. Hu, M. Ma, S. C. Huang, Y. Xiong, H. Y. Chen, L. Li and S. Peng, *Angew. Chem., Int. Ed.*, 2021, **60**, 22276-22282.

25.   Y. Zhao, Y. Gao, Z. Chen, Z. Li, T. Ma, Z. Wu and L. Wang, *Appl. Catal., B*, 2021, **297**, 120395.

26.   Y. Sun, Z. Xue, Q. Liu, Y. Jia, Y. Li, K. Liu, Y. Lin, M. Liu, G. Li and C. Y. Su, *Nat. Commun.*, 2021, **12**, 1369.

27. D. Chen, Z. Pu, R. Lu, P. Ji, P. Wang, J. Zhu, C. Lin, H. W. Li, X. Zhou, Z. Hu, F. Xia, J. Wu and S. Mu, *Adv. Energy Mater.*, 2020, **10**, 2000814.

28. D. Li, X. Chen, Y. Lv, G. Zhang, Y. Huang, W. Liu, Y. Li, R. Chen, C. Nuckolls and H. Ni, *Appl. Catal., B*, 2020, **269**, 118824.

29. Y. Li, X. Wei, L. Chen, J. Shi and M. He, *Nat. Commun.*, 2019, **10**, 5335.

30. J. Sun, W. Xu, C. Lv, L. Zhang, M. Shakouri, Y. Peng, Q. Wang, X. Yang, D. Yuan, M. Huang, Y. Hu, D. Yang and L. Zhang, *Appl. Catal., B*, 2021, **286**, 119882.

31. H. Yan, Y. Xie, A. Wu, Z. Cai, L. Wang, C. Tian, X. Zhang and H. Fu, *Adv. Mater.*, 2019, **31**, e1901174.

32. Z. Wang, L. Xu, F. Huang, L. Qu, J. Li, K. A. Owusu, Z. Liu, Z. Lin, B. Xiang, X. Liu, K. Zhao, X. Liao, W. Yang, Y. B. Cheng and L. Mai, *Adv. Energy Mater.*, 2019, **9**, 1900390.

33. Y. Zhang, B. Ouyang, J. Xu, S. Chen, R. S. Rawat and H. J. Fan, *Adv. Energy Mater.*, 2016, **6**, 1600221.

34. X. Xiao, X. K. Wang, X. X. Jiang, S. W. Song, D. K. Huang, L. Yu, Y. Zhang, S. Chen, M. K. Wang, Y. Shen and Z. F. Ren, *Small Methods*, 2020, **4**, 1900796.

35. D. Zhang, Z. Wang, X. Wu, Y. Shi, N. Nie, H. Zhao, H. Miao, X. Chen, S. Li, J. Lai and L. Wang, *Small*, 2022, **18**, e2104559.

36. L. Yu, Q. Zhu, S. Song, B. McElhenny, D. Wang, C. Wu, Z. Qin, J. Bao, Y. Yu, S. Chen and Z. Ren, *Nat. Commun.*, 2019, **10**, 5106.

37. P. Zhai, Y. Zhang, Y. Wu, J. Gao, B. Zhang, S. Cao, Y. Zhang, Z. Li, L. Sun and J. Hou, *Nat. Commun.*, 2020, **11**, 5462.

38. S. Xue, Z. B. Liu, C. Q. Ma, H. M. Cheng and W. C. Ren, *Sci. Bull.*, 2020, **65**, 123-130.

39. H. Sun, C. Tian, G. Fan, J. Qi, Z. Liu, Z. Yan, F. Cheng, J. Chen, C. P. Li and M. Du, *Adv. Funct. Mater.*, 2020, **30**, 1910596.

40. Y. T. Luo, L. Tang, U. Khan, Q. M. Yu, H. M. Cheng, X. L. Zou and B. L. Liu, *Nat. Commun.*, 2019, **10**, 269.

41. L. P. Zhang, J. T. Zhang, J. J. Fang, X. Y. Wang, L. K. Yin, W. Zhu and Z. B. Zhuang, *Small*, 2021, **17**, 2100832.

42. M. T. Jin, X. Zhang, R. Shi, Q. Lian, S. Z. Niu, O. W. Peng, Q. Wang and C. Cheng, *Appl. Catal., B*, 2021, **296**, 120350.

43. Y. Wang, G. Qian, Q. Xu, H. Zhang, F. Shen, L. Luo and S. Yin, *Appl. Catal., B*, 2021, **286**, 119881.

44. H. Liu, X. Li, L. Chen, X. Zhu, P. Dong, M. O. L. Chee, M. Ye, Y. Guo and J. Shen, *Adv. Funct. Mater.*, 2021, **32**, 2107308.

45. Y. Wang, L. Chen, X. Yu, Y. Wang and G. Zheng, *Adv. Energy Mater.*, 2017, **7**, 1601390.

46. M. Hu, H. Chen, B. Liu, X. Xu, B. Cao, P. Jing, J. Zhang, R. Gao and J. Zhang, *Appl. Catal., B*, 2022, **317**, 121774.

47. M. Ning, F. Zhang, L. Wu, X. Xing, D. Wang, S. Song, Q. Zhou, L. Yu, J. Bao, S. Chen and Z. Ren, *Energy Environ. Sci.*, 2022, **15**, 3945-3957.

48. F. Ma, S. Wang, X. Gong, X. Liu, Z. Wang, P. Wang, Y. Liu, H. Cheng, Y. Dai, Z. Zheng and B. Huang, *Appl. Catal., B*, 2022, **307**, 121198.

49. D. Shao, Q. Wang, X. Yao, Y. Zhou and X. Yu, *J. Mater. Chem. A*, 2022, **10**, 21848-21855

50. H. Sun, J. Sun, Y. Song, Y. Zhang, Y. Qiu, M. Sun, X. Tian, C. Li, Z. Lv and L. Zhang,

ACS Appl. Mater. Interfaces, 2022, **14**, 22061-22070.

51. L. Wu, L. Yu, F. Zhang, B. McElhenny, D. Luo, A. Karim, S. Chen and Z. Ren, *Adv. Funct. Mater.*, 2020, **31**, 2006484.

52. B. Wang, M. Lu, D. Chen, Q. Zhang, W. Wang, Y. Kang, Z. Fang, G. Pang and S. Feng, *J. Mater. Chem. A*, 2021, **9**, 13562-13569.

53. H. Chen, Y. Zou, J. Li, K. Zhang, Y. Xia, B. Hui and D. Yang, *Appl. Catal., B*, 2021, **293**, 120215.

54. H. Y. Wang, J. T. Ren, L. Wang, M. L. Sun, H. M. Yang, X. W. Lv and Z. Y. Yuan, *J. Energy Chem.*, 2022, **75**, 66-73.

55. X. Wang, W. Zhang, Q. Yu, X. Liu, Q. Liang, X. Meng, X. Wang and L. Wang, *Chem. Eng. J.*, 2022, **446**, 136987.

56. L. Zhang, Z. Wang and J. Qiu, *Adv. Mater.*, 2022, **34**, e2109321.

57. F. Sun, J. Qin, Z. Wang, M. Yu, X. Wu, X. Sun and J. Qiu, *Nat. Commun.*, 2021, **12**, 4182.

58. T. Cui, J. Chi, J. Zhu, X. Sun, J. Lai, Z. Li and L. Wang, *Appl. Catal., B*, 2022, **319**, 121950.

59. T. Cui, X. Zhai, L. Guo, J. Chi, Y. Zhang, J. Zhu, X. Sun and L. Wang, *Chin. J. Catal.*, 2022, **43**, 2202-2211.